Microanalysis for Oxygen Fugacity

by Secondary Ion Mass Spectrometry

by

Sarah Marie Dillon

A Thesis Presented in Partial Fulfillment
of the Requirements for the Degree
Master of Science

Approved April 2019 by the
Graduate Supervisory Committee:

Richard Hervig, Chair
Dan Shim
Peter Williams

ARIZONA STATE UNIVERSITY

May 2019

ABSTRACT

Oxygen fugacity (fO_2) is a thermodynamic variable used to represent the redox state of a material or a system. It is equivalent to the partial pressure of oxygen in a particular environment corrected for the non-ideal behavior of the gas. fO_2 is often used to indicate the potential for iron to occur in a more oxidized or reduced state at a particular temperature and pressure in a natural system. Secondary ion mass spectrometry (SIMS) is a powerful analytical instrument that can be used to analyze elemental and isotopic compositional information about microscopic features within solid materials. SIMS analyses of the secondary ion energy distribution of semi-pure metals demonstrate that the energy spectrum of individual mass lines can provide information about alterations in its surface environment.

The application of high-resolution (see Appendix C) energy spectrum calibrations to natural ilmenite led to the investigation of zirconium ($^{90}Zr^{+}$) and niobium ($^{93}Nb^{+}$) as potential indicators of sample fO_2. Energy spectrum measurements were performed on an array of ilmenite crystals from the earth's upper mantle retrieved from kimberlites and from a reduced meteorite. In all studied materials, variability in the peak shape and width of the energy spectra has been correlated with inferred sample fO_2. The best descriptor of this relationship is the full-width at half-maximum (FWHM; see Appendix C) of the energy spectra for each sample. It has been estimated that a 1eV change in the FWHM of $^{93}Nb^{+}$ energy spectra is roughly equivalent to 1 log unit fO_2. Simple estimates of precision suggest the FWHM values can be trusted to ± 1eV and sample fO_2 can be predicted to ±1 log unit, assuming the temperature of formation is known.

The work of this thesis also explores the applicability of this technique beyond analysis of semi-pure metals and ilmenite crystals from kimberlites. This technique was applied to titanium oxides experimentally formed at known fO_2 as well as an ilmenite crystal that showed compositional variations across the grain (i.e., core to rim chemical variations). Analyses of titanium oxides formed at known fO_2 agree with the estimation that 1 eV change in the FWHM of $^{93}Nb^{+}$ is equivalent to ~1 log unit fO_2 (in all cases but one); this is also true for analyses of a natural ilmenite crystal with compositional variations across the grain.

Dedicated to Sean,

Thank you for always inspiring me to suceed no matter how tough times get.

ACKNOWLEDGMENTS

I am very grateful to the people I have been associated with throughout my graduate program. Foremost is my graduate advisor, Dr. Richard Hervig, who has helped me gain a greater appreciation for analytical tools. His insightful discussions provided a wealth of information for me. I am also indebted to Drs. Peter Williams and Dan Shim who have been like additional advisors to me.

Although I am not directly involved with this research group, I would like to thank the Experimental Petrology and Igneous Processes Center (EPIC) for welcoming me into their group and making my stay at ASU more enjoyable; Thank you, Hannah, Kara, Meghan, Kayla, and Christy, among others.

I would also like to thank my wonderful husband, Holden. Your love, support, and patience has been everything to me. I couldn't have done this without you.

I am very thankful for the support from NSF (EAR1352996) and those who provided samples for this work. A special thank you is dedicated to the late J. Barry Dawson who provided a bulk of the samples used throughout this project. I would also like to thank Dr. Phil Janney at the University of Cape Town, South Africa and Megan Holycross at the Smithsonian Institute for lending additional samples used in this work.

TABLE OF CONTENTS

Page

CHAPTER Page

LIST OF TABLES

LIST OF FIGURES

Figure Page

LIST OF EQUATIONS

CHAPTER 1

INTRODUCTION

1.1 MANTLE GEOCHEMISTRY

The solid Earth consists of three distinct layers: crust, mantle, and core. The largest component of these three layers is the mantle, which makes up 67% of the Earth by mass and 88% by volume (White, 2013). Although direct collection of mantle material is impossible due to depth, pressure, and heat, the mantle can be sampled where it has been tectonically exposed or where mantle xenoliths are carried to the surface by volcanic eruptions. It is important to note that volcanism and tectonics are only capable of sampling the uppermost mantle; even the most deeply generated magmas (i.e., kimberlites) originate from the upper 400 km of the mantle. The mantle composition below ~400 km is predicted from seismic velocity profiles, density profiles, and high P-T experiments (see Appendix A for more mantle profile information).

The mantle is described as being heterogenous on all scales and consists of multiple reservoirs like the upper and lower mantles (White, 2013). Heterogeneity in the mantle is not limited to just chemical or mineralogical variations; a number of discontinuities also exist in the density and seismic velocity profiles of the mantle. Some of these discontinuities represent compositional changes like those seen at the crust-mantle and core-mantle boundaries while others represent isochemical phase changes due to pressure and temperature changes (See Appendix B for mantle mineralogy).

In the uppermost 200 km of the mantle, aluminous phases change with increasing pressure; plagioclase ($CaAl_2Si_2O_8$ or $NaAlSi_3O_8$) changes to spinel ($MgAl_2O_4$), and then changes to garnet ($X_3Y_2(SiO_4)_3$, where X is (Ca, Mg, Fe, or Mn)$^{2+}$ and Y is (Al, Fe,

$Cr)^{3+}$) (McDonough & Rudnick, 1998). The garnet phase, garnet lherzolite, remains stable at depths up to 300 km where significant amounts of pyroxenes begin to dissolve in garnet, forming a high pressure garnet phase known as majorite, with a general composition of $M_2(MSi, Al_2)Si_3O_{12}$ (M is Mg, Fe, or Ca) (McDonough & Rudnick, 1998). This phase is stable at depths up to about 460 km (see Appendix A).

Between 410 and 670 km exists a seismic velocity discontinuity known as the mantle transition zone (see Appendix A and B for transition zone information). This transition zone represents depths at which numerous major phase changes occur in several minerals due to an effect of increased pressure and temperature. It is known as the transition zone because olivine ($(Mg, Fe)_2SiO_4$) undergoes several phase transitions that mark major seismic discontinuities. The first phase transition occurs around 400 km when olivine undergoes an exothermic phase transition from its α-form to its β-form (i.e., wadsleyite). At a depth of around 520 km wadsleyite transforms exothermically into ringwoodite (γ-form; γ-olivine), which exists in a spinel structure. Additional phases within the transition zone, like majorite, begin to exsolve Mg and Ca to form $CaSiO_3$ in the perovskite ($CaSiO_3$) structure and $MgSiO_3$ in the ilmenite ($FeTiO_3$) structure until the majorite phase disappears around 720 km (McDonough & Rudnick, 1998).

Around 660 km a sharp increase in seismic velocity marks an area known as the 660 seismic discontinuity. This depth represents the uppermost portion of the lower mantle and is marked by major phase changes. At this depth, Mg_2SiO_4 is no longer stable in its previous structure as ringwoodite (γ-olivine) and it decomposes into the silicate perovskite structures magnesiowüstite ($(Mg, Fe)SiO_3$) and ferropericlase ($(Mg, Fe)O$) in

an endothermic reaction (with Fe preferentially going into the magnesiowüstite structure) (McDonough & Rudnick, 1998).

The lower mantle is represented by a much less accessible area between the 660 km seismic discontinuity and the core-mantle boundary at 2900 km. Some diamond inclusions containing lower mantle assemblages have been discovered, but these provide little compositional constraints, so the composition of the lower mantle must be studied indirectly through experimentation and geophysical measurements.

1.2 KIMBERLITES

Kimberlites are an unusual igneous phenomenon that occur in the Earth's crust in vertical structures known as kimberlite pipes, as well as igneous dykes or horizontal sills (Figure 1.2.1). Kimberlites are said to form within the mantle at depths between 150-450 km (Patterson & Francis, 2013). It is this depth of melting and generation that makes kimberlites prone to hosting diamond xenocrysts and peridotite mantle xenoliths (i.e., inclusion of mantle rocks and minerals in the kimberlitic magma). Petrographically, kimberlites are complex rocks; the magma composition reflects depletions in silica and enrichment of incompatible trace-elements (Mitchell, 1986). Kimberlites have the potential to provide information about the composition of the mantle and melting processes occurring at or near the interface between the cratonic continental lithosphere and the underlying convecting asthenospheric mantle.

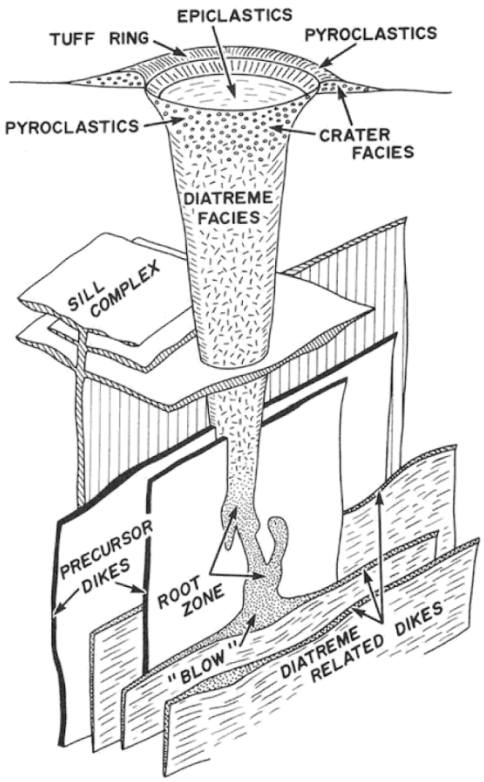

Figure 1.2.1. Model of an idealized kimberlite magmatic system. Hypabyssal facies rocks include sills, dikes, root zone, and "blow" (Mitchell, 1986)

Mantle derived xenoliths and xenocrysts. It should be noted that although great reliance is placed on xenolith suites for interpretation of the mineralogy and petrology of the upper mantle, xenolith suite sampling is limited to what mantle materials have been brought to the surface of the earth by geologic processes. Many xenoliths found in kimberlites vary compositionally and are often separated into compositional groups. Xenolith suites recognized by Dawson (1980) include the peridotite-pyroxene suite, eclogites and grosspydites, metasomatized peridotites containing potassic richterite (i.e., K-richterite) and/or phlogopite, glimmerites, and the MARID (Mica-Amphibole-Rutile-Ilmenite-Diopside; Dawson & Smith, 1977) suite of rocks (Mitchell, 1986). MARID suite xenoliths are rare and known primarily from South Africa (Dawson & Smith, 1977).

Xenocrysts are often added to kimberlitic magma by fragmentation or disintegration of xenoliths during transport. Some xenocrysts are easy to recognize due to their compositional similarities with minerals in xenoliths, but compositional overlap with minerals crystalizing in the kimberlite magma (e.g., olivine or phlogopite) may make xenocryst identification and distinction impossible.

Megacrysts. Megacrysts or discrete nodules (Boyd & Nixon, 1975) are large (> 2.0 cm) single crystals that are widespread and sometimes abundant as inclusions in kimberlites (Dawson, 1980). It is assumed that these minerals are so large that they could not be mantle xenocrysts, which range in grain size from 2-4 mm. Dawson (1980) describes two distinct series of megacrysts: chromium rich (fairly rare; higher Mg and Cr) and chromium poor (more common; higher Ti and Fe). The chromium poor megacrysts are common in South African kimberlites and include large crystals of olivine, orthopyroxene, clinopyroxene, garnet, and ilmenite (Dawson, 1980). Course-grained lamellar intergrowths of pyroxene (especially clinopyroxene) and ilmenite are common, as are small inclusions of one phase within larger crystals of another (Mitchell, 1986).

Ilmenite. It should be assumed that ilmenite crystals from kimberlites are not all formed in a single process. Xu, Melgarejo, and Castillo-Oliver (2018) defined several different textural-compositional types of ilmenite based on petrographic and compositional studies. The ilmenite generations record different processes in the kimberlite's history from the mantle to the Earth's surface.

The first generation of polycrystalline Mg-rich ilmenites are assumed to be produced by metasomatic processes in the mantle before emplacement of the kimberlite (Xu et al., 2018). Fragmentation of the polycrystalline aggregates results in rounded megacrysts of ilmenite with a similar Mg-rich composition. Interaction of these rounded ilmenite megacrysts with fluids results in the replacement along grain boundaries and cracks of pre-existing ilmenite with geikelite ($MgTiO_3$). Later ilmenite generation compositions are characterized by enrichment of particular elements by replacement or by late-stage petrogenetic processes. Ilmenite replacing other oxide minerals is common and results in enrichment of elements from that oxide; for example, if ilmenite were to replace eskolaite (Cr_2O_3) the resultant ilmenite would be enriched in Cr. Xu et al. (2018) suggests that the last generation of ilmenite to form would be produced by late replacement of groundmass minerals such as ulvöspinel or other Ti-rich minerals.

1.3 OXYGEN FUGACITY (fO_2)

Iron is the fourth most abundant element in the solar system. Due to its nature as a transition element with the ability to exist in multiple valence states, iron can have an effect on the physical and chemical properties of natural rocks and minerals. Because iron can exist in three oxidation states, some variable must be used in geologic systems to indicate the potential for iron to occur in a more oxidized or reduced state (Frost, 1991a).

fO_2 is a thermodynamic variable used to represent the redox state of a system. It is equivalent to the partial pressure of oxygen in a particular environment corrected for the non-ideal behavior of the gas. fO_2 is often used to indicate the potential for iron to occur in a more oxidized or reduced state at a particular temperature or pressure in a

natural system and it is measured by the free energy change between the oxidized and reduced portions of an assemblage in a rock. fO_2 is referred to in terms of stability fields of minerals like fayalite, magnetite, and hematite. These stability fields are used to determine whether iron is likely to be found in its native (Fe^0) state, as a divalent (Fe^{2+}) ion in a silicate, or as a divalent or trivalent (Fe^{3+}) ion in an oxide (Frost, 1991a). At very low fO_2, such as those found in Earth's silica bearing systems, iron can occur as a divalent cation (i.e., ferrous) and is incorporated mostly into silicates (Frost, 1991a). As fO_2 increases, iron may be present in both the divalent (i.e., ferrous) and trivalent (i.e., ferric) states; At very high fO_2, iron occurs in the ferric state. The reactions governing the change of iron from native to ferrous to ferric states are shown in equations 1.1-1.6 below (from Frost, 1991a). These reactions represent a particular fO_2 value and are referred to as fO_2 buffers.

$$2\ Fe + SiO_2 + O_2 = Fe_2SiO_4 \qquad \text{(1.1) QIF}$$
$$\text{Iron + Quartz + } O_2 \text{ = Fayalite}$$

$$2\ (1\text{-}x)\ Fe + O_2 = 2Fe_{1-x}O \qquad \text{(1.2) IW}$$
$$\text{Iron + } O_2 \text{ = Wüstite}$$

$$3\ Fe_{1-x}O + O_2 = Fe_3O_4 \qquad \text{(1.3) WM}$$
$$\text{Wüstite + } O_2 \text{ = Magnetite}$$

$$3\ Fe_2SiO_4 + O_2 = 2\ Fe_3O_4 + 3\ SiO_2 \qquad \text{(1.4) QFM}$$
$$\text{Fayalite + } O_2 \text{ = Magnetite + Quartz}$$

$$2\ Ni + O_2 = 2\ NiO \qquad \text{(1.5) NiNiO}$$
$$\text{Nickel + } O_2 \text{ = Nickel oxide}$$

$$4\ Fe_3O_4 + O_2 = 6\ Fe_2O_3 \qquad \text{(1.6) MH}$$
$$\text{Magnetite + } O_2 \text{ = Hematite}$$

These buffers are plotted in thermodynamic space in Figure 1.2.2 based on their log fO_2 vs. temperature at 1 bar pressure; the buffers are plotted from algorithms compiled by Frost (1991a). An important feature to note in Figure 1.2.2 is that the oxygen fugacity of all the buffers increases as temperature increases. This is because fO_2 reflects devolatilization of the reactions (Frost, 1991a); for an fO_2 buffer, devolatilization indicates the release of oxygen, resulting in the subsequent increase in fO_2. Another important feature is related to the slope of the oxygen buffers in log fO_2 – T space. This is due to an equal enthalpy change for all the buffers associated with increasing oxidation (Frost, 1991a).

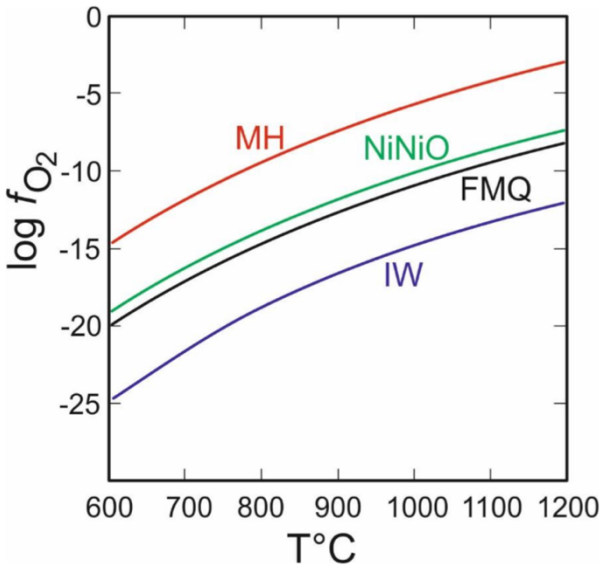

Figure 1.2.2. Log oxygen fO_2 vs. temperature at 1 bar pressure for common buffer assemblages (modified after Frost, 1991a).

Although the various buffers are an important means by which one can orient themselves in oxygen fugacity space, the buffers listed above rarely exist in nature (Frost, 1991a). It is important to understand the difference between the behavior of fO_2 in an experimental charge and in geologic systems. To distinguish this behavior, the fO_2 of a

rock is described as 'equilibrated at oxygen fugacities equivalent to those of a particular buffer'. This suggests that the rock's fO_2 is not equal to the buffer but is equivalent to the range of P-T conditions in which that buffer is stable.

In natural systems, oxygen fugacity is internally controlled by multivariant equilibria involving the silicates, the oxides, and, in igneous rocks, the melt. Thus, fO_2 is not fixed, but varies to accommodate the dictates of the phase compositions. The presence of Mg and Ti can play an important role in determining the relative stabilities of silicates and some oxides. Mg and Fe^{2+} substitute for each other in a variety of silicate minerals and the solution of Mg into Fe^{2+}-silicates stabilizes them to higher fO_2. Some Fe^{2+}-bearing silicates can even be stable in the presence of hematite (MH) if they've incorporated enough Mg (Frost, 1991a). Coupled substitution of Ti and Fe^{2+} for Fe^{3+} in both magnetite and hematite will stabilize these oxides relative to silicates.

In an assemblage containing both silicates and oxides, the Fe/Mg ratio of the silicates, the Ti content and the Fe^{3+}/Fe^{2+} ratio of the oxides, and fO_2 are all interrelated. In many rocks it is appropriate to assume fO_2 is a function of the Fe/Mg ratio of the silicates and the Ti content of the oxides. This is because it is more likely that fO_2 is a variable that is governed by the mineral assemblage in the rock rather than one that is imposed from the environment (Frost, 1991a).

Oxygen Fugacity in the Mantle. Free oxygen in petrologic environments, like the mantle, is never present in great quantities. In a condensed system (like a fluid-free system) the partial pressure of oxygen has no physical meaning. In contrast, fO_2 can be used to describe a condensed system because it controls the chemical potential (Frost,

1991a). Oxygen fugacity can affect subsolidus and supersolidus phase relations, the presence of speciation of a fluid phase, transport properties such as electrical conductivity, diffusivity, and mechanical behavior. Sources of oxygen in natural systems (especially igneous and metamorphic systems) may be through the disassociation of H_2O, CO_2, or SO_2, the reaction of N_2 to NH_3 in aqueous fluids, the precipitation of Fe^{3+}, or other reactions that could take place in the system of interest.

Most igneous rocks have equilibrated within a few log units of fO_2 to the QFM buffer (Haggerty, 1976). The fO_2 at which mafic rocks equilibrate (i.e., crystallized) range from about two log units below QFM to more than four log units below QFM when native iron is present (Ulff-Møller, 1985). Most felsic rocks crystalized at fO_2 1-2 log units above QFM, although a few silicic rocks equilibrated at fO_2 more than three units above QFM (Haggerty, 1976).

Metamorphic rocks have a wider range in fO_2 than igneous rocks. This is partially a result of the wider range of bulk compositions found in metamorphic rocks (Frost, 1991b). The relative range of fO_2 found in metamorphic rocks is around 10 log units. Some metamorphic rocks range from the MH buffer (5-6 log units above QFM) to the IM buffer (5-6 log units below QFM) (Frost, 1991b).

It is well known that mantle phases in the iron-free system MgO-SiO_2-H_2O can incorporate significant quantities of OH in their crystal structures. Hence, Iron, in particular Fe^{3+}, is not required to stabilize OH. Nevertheless, McCammon et al. (2004) showed that there is a relation between $Fe^{3+}/\sum Fe$ and the incorporation of OH in high-pressure mantle phases. Although the $Fe^{3+}/\sum Fe$ ratio is not a simple function of fO_2, this ratio is often used to monitor fO_2 in melts and glasses. It can also be used as an indicator

of fO_2 in volcanic rocks that are assumed to be free of cumulate minerals (Frost, 1991a). In many rocks, fO_2 is monitored by mineral equilibria (i.e., dependent on mineral composition) rather than the $Fe^{3+}/\sum Fe$ ratio. This is because the $Fe^{3+}/\sum Fe$ ratio is strongly dependent on the relative proportions of phases in a rock while fO_2, an intensive variable, is independent of this.

The relation between $Fe^{3+}/\sum Fe$ is non-uniform and varies with pressure, temperature, and compositional changes throughout the mantle. In the upper mantle, fO_2 is relatively high; measurements from xenoliths show an average fO_2 of QFM -1 (i.e., 1 log unit below the QFM buffer) (Wood, 1991). Despite the relatively high fO_2, the bulk $Fe^{3+}/\sum Fe$ of the upper mantle is low ($Fe^{3+}/\sum Fe \sim 3\%$; O'Neill & Wall, 1987). The mineral olivine may be responsible for this low Fe^{3+} in the upper mantle. Olivine, which makes up around 60% of the upper mantle, almost completely excludes Fe^{3+} due to unfavorable energetics of defect formation on anhydrous olivine. Spinel, however, contains significant amounts of Fe^{3+} ($Fe^{3+}/\sum Fe \sim 50\%$; McCammon et al., 2004) which relates to a high fO_2. At greater depths, laboratory experiments have shown a relation between the increased affinity of high-pressure phases for Fe^{3+} and lower fO_2 (McCammon et al., 2004).

The relation between $Fe^{3+}/\sum Fe$ and oxygen fugacity is reversed in the lower mantle. (Mg, Fe)(Si, Al)O_3 perovskite, which constitutes at least 80% of the lower mantle by volume, incorporates significant Fe^{3+} due to the favorable energetics of trivalent cation substitution in the structure (McCammon et al., 2004). For a pyrolite bulk composition, $Fe^{3+}/\sum Fe$ of (Mg, Fe), (Si, Al)O_3 perovskite is estimated to be approximately 50%, regardless of oxygen fugacity (Lauterbach, McCammon, Van Aken,

Langenhorst, & Seifert, 2000). This represents more than a 10-fold increase in Fe^{3+} concentrations at the top of the lower mantle. Although the oxygen fugacity of the bulk lower mantle is still an open question, a relatively reduced lower mantle would be more compatible with existing evidence that the upper mantle was extremely oxidized.

The overall picture of oxygen fugacity within the mantle is therefore a general decrease with depth, and no evidence for a significant discontinuity in oxygen fugacity between the transition zone and the lower mantle. In contrast, the bulk concentration of Fe^{3+} is low throughout the upper mantle, and (likely) the transition zone, but increases dramatically near the top of the lower mantle as (Mg, Fe)(Si, Al)O_3 perovskite becomes more stable. The influence of such an increase in the abundance of Fe^{3+} is greatest for processes that involve an exchange of material through the garnet-perovskite transformation (e.g., subduction and mantle upwelling) where the question of electrostatic charge must be addressed (McCammon et al., 2004).

Oxides in the Mantle. In terms of its constituent elements, the mantle is made up of around 44.8% oxygen, 21.5% silicon, and 22.8% magnesium (Cain, 2016). There is also iron, aluminum, calcium, sodium, and potassium. These elements are bound together in the form of silicate rocks which take the form of oxides in the mantle. The most common oxide is silicon dioxide (SiO_2) at 48% followed by magnesium oxide (MgO) at 37.8% (Cain, 2016). Metasomatism of these xenoliths results in hydrous alteration of their mineral constituents which can result in abnormal trace element enrichment patterns (cryptic metasomatism) or with the appearance of replacement minerals (modal metasomatism) (Dawson, 1984). Metasomatized xenoliths are often characterized by the

presence of phlogopite, amphibole, apatite, mineral oxides, carbonate, and sulfides (Haggerty, 1995).

Dawson and Smith (1977) suggest that rocks of the MARID suite crystallized under oxidizing conditions from a metasomatic melt chemically similar to the kimberlite. Members of the ilmenite ($FeTiO_3$)-geikelite ($MgTiO_3$)-hematite (Fe_2O_3) series are prominent among the megacrysts in many kimberlites (Haggerty, 1991). Solid solution of the pyrophanite ($MnTiO_3$) member is typical of carbonated kimberlites, lamproites, and as a groundmass constituent in carbonatites. Because the redox state of the upper mantle is approximately QFM (Wood, 1991), and because the ilmenite-geikelite-hematite series has a ternary solvus (Figure 1.2.3), the distribution of compositions is largely between ilmenite-geikelite, is limited between ilmenite-hematite, and is virtually absent between geikelite-hematite.

Exsolution within the ilmenite series is relatively rare, but subsolidus reduction of ilmenite solid solutions to chromian titanomagnetite is common. Ilmenite is used as a prospective guide for kimberlites because the mineral has distinctively high MgO content, coupled with moderate to high Cr_2O_3 (eskolaite) concentrations. Although the depths of origin of ilmenite megacrysts remain uncertain, two observations are noted: higher MgO content is indicative of diamonds, and low MgO ilmenites enriched in Fe^{2+} and Fe^{3+} serve as an index of the redox environment. Ilmenite members are widespread in metasomatic associations; as veins in harzburgites and lherzolite substrates, as veins in discrete clinopyroxene, as intergrowths or reaction rims on metasomatic rutile, or in association with the exotic mineral oxide suite (Haggerty, 1995). Ilmenite is an essential

constituent of MARID xenoliths and compositions are substantially more magnesian in these associations.

Rutile is diagnostic of metasomatic assemblages (Haggerty, 1995). Although rutile is an essential constituent of MARID rocks, concentrations vary immensely; possibly, as a result of the reaction of rutile with Fe^{2+} bearing silicates (or melt) to form ilmenite. Other reactions between rutile and spinel produce members of the exotic oxide suite in which rutile is present as an accessory phase. Rutile is rarely of endmember composition with many rutiles reported to be Fe-rich, but this could be due to incorporated submicroscopic ilmenite (Haggerty, 1995). Other significant element proportions are Cr and Nb (but not Ta) with maximum concentrations of 8 wt% Cr_2O_3 and 21 wt% Nb_2O_5.

Exotic mineral oxides are termed as exotic because of the unusual association of large ion lithophile elements (LILE: K, Ba, Ca, Sr, Na) and high field strength elements (HFSE: Ti, Zr, Nb, REE). Haggerty (1991) recognized two groups of exotic mineral oxides in upper mantle metasomatized xenoliths. The first group has the rhombohedral crichtonite structure with a general formula $AM_{21}O_{38}$ (where A are LILE cations and M are smaller HFSE cations). The second group has the hexagonal magnetoplumbite structure and the general formula $AM_{12}O_{19}$ (where A and M have a similar disposition to the crichtonite elements; Haggerty, 1995).

Ilmenites and Oxygen Barometry. Temperatures and oxygen fugacities reported by Haggerty and Tompkins (1983) on ilmenite megacrysts in kimberlites demonstrate a source region in the upper mantle that is moderately oxidized; but not all ilmenites will

reflect the same magmatic history or fugacity. fO_2 is an important parameter to constrain in order to understand magmatic evolution histories. Numerous methods based on various principles have been developed with the aim to reconstruct magmatic fO_2 (i.e., oxygen barometers). Many oxygen barometers, like that of Buddington and Lindsley (1964) and Frost and Lindsley (1991), are based on mineral equilibria. By far the most commonly used oxybarometer in crustal rocks is based on the equilibrium composition of Fe–Ti oxides. Buddington and Lindsley (1964) proposed the use of the compositions of coexisting ilmenite-hematite and magnetite-ulvöspinel solid solutions in the system FeO-Fe_2O_3-TiO_2 as a geothermometer and oxygen barometer. This mineral system is shown in Figure 1.2.3.

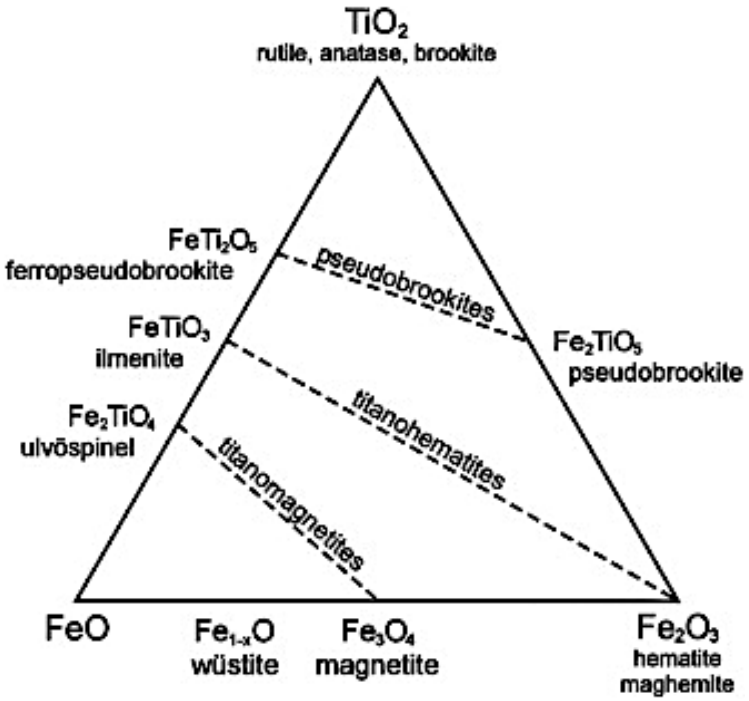

Figure 1.2.3. Phases in the system FeO-Fe_2O_3-TiO_2, showing the major solid solution series magnetite-ulvöspinel, hematite-ilmenite, and pseudobrookite-$FeTi_2O_6$ in mole percent (modified after Buddington & Lindsley, 1964).

Thermodynamic equilibrium methods have been used to develop several oxygen barometers from the experimental data of Buddington and Lindsley (1964). Powell and Powell (1977) developed an independent Fe-Ti oxide geothermometer and oxygen barometer (presented graphically in Figure 1.2.4) for coexisting ilmenite solid solution and magnetite solid solution in the system FeO-Fe_2O_3-TiO_2.

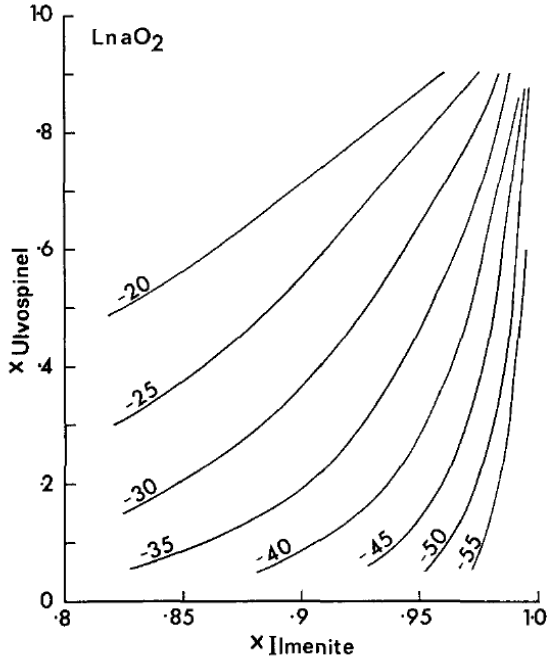

Figure 1.2.4. Oxygen barometer presented terms of x_{ulv} and x_{ilm} contoured for the ln aO_2. The geobarometer is more sensitive to the composition of ilmenite than it is to the composition of magnetite (modified after Powell & Powell, 1977).

The graphical geothermometer and oxygen barometer in Figure 1.2.4 can only be applied to natural coexisting Fe-Ti oxides that depart little from the FeO-Fe_2O_3-TiO_2 system. The composition of the coexisting phases is a monitor of both the temperature and fO_2 at which they equilibrated (i.e., the Fe-Ti oxide thermometer and oxygen barometer; Buddington & Lindsley, 1964). Ilmenite exists within this system, and is therefore, a naturally occurring Fe-Ti oxide that can be analyzed to determine the fO_2 of

crystallization. Although, natural deviations from this system, like enrichment of trace elements or mineral intergrowths, could increase the uncertainty of the calculated fO_2.

Additional oxygen barometers have been proposed, but due to the complexity of ilmenite equilibria compositions, not every oxygen barometer will accurately measure the fO_2. In this thesis, I present a technique that has the potential to measure the oxygen fugacity of ilmenites that were equilibrated and crystalized in different environments. Though no absolute fO_2 values can be measured with this technique due to the lack of standard materials, a relative idea of sample fO_2 can be interpreted. This technique has the potential to be used as a "pre-scan" to give researchers an idea of fO_2 variations in the sample that may be of interest or identify areas in the sample that require analysis by other analytical techniques.

CHAPTER 2

TECHNIQUE DEVELOPMENT

2.1 SECONDARY ION MASS SPECTROMETRY (SIMS)

SIMS instruments are powerful analytical instruments that can be used to analyze the elemental and isotopic composition of solid materials. The technique of mass selecting secondary ion microscopy was introduced by Castaing and Slodzian in 1962. A secondary ion mass spectrometer utilizes a primary ion beam of energetic ions to remove both neutral and ionized atoms from the sample surface (this process is also known as "sputtering"). The ions removed from the sample are accelerated to keV energies through the secondary column of the instrument where they are energy selected and mass analyzed in the mass spectrometer (Hinton & Long, 1979).

2.1.1 The ASU Cameca IMS-6f SIMS. SIMS measurements of the secondary ion energy distribution of elements and oxides in natural ilmenites and semi-pure metals were made by Dr. Richard Hervig and myself using the ASU Cameca IMS-6f SIMS instrument. This is a commercial instrument that has been modified so we may conduct analyses using a primary ion beam of Argon (specifically, Ar^+). Since this thesis explores the energy distributions of secondary ions, I present a description of the general operation principles of the instrument.

The primary ion beam. In the ASU Cameca IMS-6f there are 2 primary ion sources; a Cesium source, which produces a Cs^+ beam, and a duoplasmatron. The duoplasmatron is capable of producing positive or negative ion beams of a variety of

atomic and molecular species (e.g., $^{16}O^{+}$, $^{16}O_2^{+}$, $^{16}O^{-}$,$^{40}Ar^{+}$, etc.). Both ion sources are floated at a high electrical potential (up to ±15 kV for the duoplasmatron) and the ion beam is extracted by a conical lens held at ground. Once the beam is extracted from the duoplasmatron, it passes through the primary beam mass filter (PBMF; a small mass spectrometer for selecting a primary ion with only one mass/charge ratio). It is then passed through the ion optical system of the primary column where the beam is shaped and focused via a series of three electrostatic lenses, deflectors, stigmators and apertures. The primary ion optics also control the primary beam current. For the purpose of this research, a primary ion beam of argon ($^{40}Ar^{+}$) was predominantly used. The primary ions were accelerated to high energies (+12.5 keV) and then projected at the sample surface. After passing through the ion optical system, the beam impacts a sample held at a particular electrical potential (in this case, our sample is held at +5 kV).

The secondary ion source. The impact of the primary ion beam on the sample triggers a cascade of atomic collisions which may result in the ejection of one or more atoms from the upper-most layers of the sample (Castaing & Slodzian, 1981). This interaction between the primary ion beam and the sample surface is known as "sputtering". During the sputtering process, a fraction of the ejected particles are ionized; these secondary ions are comprised of positive, negative, monatomic, and polyatomic ions. In the Cameca design, secondary ions are accelerated up to an energy of several keV by the difference between the sample potential and a grounded plate ~5 mm in front of the sample, and the ions are transmitted into the mass spectrometer as described below.

The secondary ion optics. The IMS-6f used throughout this study is classified as a forward-geometry instrument; this indicates that secondary ions will pass through an electrostatic analyzer (ESA) before they pass through the magnetic analyzer (sector). This allows the ESA to reduce the energy range of the secondary ions before they're separated into independent ion beams (based on mass-to-charge ratios; see Appendix C) in the magnetic sector (Meuller & Vervoort, 2017).

The sputtered ions are made into a beam suitable for input into the mass spectrometer by action of the ion acceleration/extraction system and the transfer optics. The secondary ion extraction system consists of a flat, conducting sample surface that is maintained at a potential variable from a few hundred volts to ±10,000 V. In this study we used +5000 V on the sample and a grounded electrode with a circular hole parallel to the sample at a distance of 5 mm. The primary ion beam enters through a hole in the extraction electrode at 30^{o} to the optical axis (normal to the sample surface). Secondary ions are accelerated along the optical axis by an electrostatic field from the extraction electrode. The grounded extraction electrode is the first of many elements that comprise the transfer optics. The transfer optics consist of electrostatic lenses, meaning the ion trajectories through these secondary ion optics are independent of mass to charge (m/z) (Slodzian, 1975).

The transfer optics are able to transform the virtual images formed by the extraction electrode into real magnified images of both the sample surface and the crossover to optimize sensitivity by allowing magnification of the total analyzed area (i.e., image fields). There are three discreet, user-definable magnifications available, corresponding (in our case) to the maximum image fields of ~250 µm, 150 µm, and 75

μm. Although spatial resolution is lost with increased magnification of the sample, for certain applications (e.g., rare earth elements or H isotopic analyses) it is desirable to have increased sensitivity. Apertures are placed near the focal planes of the electrostatic analyzer (ESA) and the entrance slit to the mass spectrometer. These apertures work to limit the geometric extent of the ion beam (improve resolution; see Appendix C). The field aperture transmits only ions originating from a selected area of the sample surface, while the contrast aperture restricts the size of the crossover, thereby improving the spatial resolution of the ion image.

The mass spectrometer is a double-focusing type, meaning the instrument focuses ions with both an energy spread and angular spread. The electrostatic sector analyzer (ESA) consists of two concentric spherical plates that are held at opposite potentials. Ions pass through the electric field between these two plates where they are dispersed based on their energy. Ions leaving the entrance slit with an angular spread are refocused by the spherical ESA in the plane of the energy slit. Ions with different energies are dispersed at the energy slit, which can be used to select a specific ion energy range to transmit to the magnet, which refocuses the ions at the exit slit. The magnet also refocuses at the exit slit ions diverging in angle, achieving a “double focus”.

In the image plane of the ESA (before the spectrometer lens) a slit is placed that can be used to select an energy band up to ~130 eV wide. This energy slit is employed to reduce chromatic aberrations for high mass resolution (see Appendix C) measurements and also can be used to discriminate against complex molecular ions (which have energy distribution different from atomic ions) in the technique known as “energy filtering”

(Zinner & Crozaz, 1986). Once ions are energy filtered, they travel into the magnetic analyzer sector where they are filtered by m/z.

The magnetic analyzer separates ions based on their mass-to-charge ratios. A deflector and stigmator are placed before the exit slit of the magnetic sector to tune the peak shapes and align the images of the sample and crossover with respect to the projection optics.

The ion detection systems. The image of the sample surface transported by the spectrometer is virtual and in order to view this, it must be converted to a real image. This is accomplished by a pair of electrostatic lenses called the projection optics. By changing the focal length of the projector, it is possible to vary the final magnification of the image or, alternatively, to project a magnified image of the exit slit (i.e., the crossover) onto a channel plate detector. Ions striking the grounded face of this detector eject secondary electrons which are multiplied with small channels. The gain is controlled by varying the potential difference across these micro-channels. After exiting the channels, the electrons are accelerated and hit a fluorescent screen, thereby producing an optical image. A deflector after the projector lens is used to center the respective image on the channel plate.

There are also detectors to quantitatively measure the total intensity of the mass filtered ion beam. After projection optics, there is a spherical electrostatic sector that, when energized, deflects the ion beam by 90^{o} toward either a faraday cup (FC) or the electron multiplier (EM). The EM is used in a pulse counting mode; a counter monitors the secondary ion signal at 10 ms intervals and automatically causes the FC to be inserted

into the beam path for intensities exceeding 10^6 ions s^{-1} in order to protect the EM from current overload.

2.1.2 Energy Spectra. SIMS analyses can reveal surface compositional details down to a micrometer size, analyze thin films, and provide composition-versus-depth profiles (Rudat & Morrison, 1979). Some of the most common analytical approaches with SIMS instruments is to monitor changes in the mass spectrum or to monitor changes in the individual mass line spectrum. Another important source of information may be represented by energy spectra of individual secondary-ion mass lines. The shape of an energy spectrum can provide clues about the surface binding energy and the ionization mechanism of the ion. Changes in the shape of the energy spectrum as the ion bombardment conditions are varied can provide information about the alterations in the surface environment (such as oxidation) (Rudat & Morrison, 1979).

To obtain energy spectra of many elements, the instrument must first be calibrated so the ESA provides high energy resolution and the ion optics at the entrance slit, exit slit, and energy window of the mass spectrometer provide high mass resolution. The spectra are obtained by varying the sample potential by small voltage steps and measuring the detector pulse count rate at each energy (Rudat & Morrison, 1979). Figure 2.1.1 shows a typical energy distribution for secondary ions.

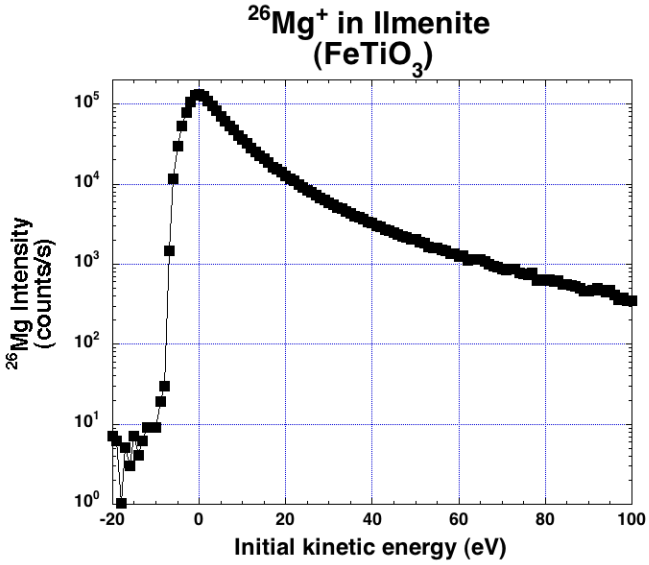

Figure 2.1.1. The energy distribution (spectrum) for $^{26}Mg^+$ secondary ions. The axes of this plot are magnesium ion intensity versus an applied voltage offset from 9000 V.

In Figure 2.1.1, the intensity of $^{26}Mg^+$ ions are shown as a function of the acceleration potential. This potential is varied around the central potential of 9 kV. The offset of -20 V $\rightarrow$ +100 V would consequently refer to changing the accelerating potential from 9020 V $\rightarrow$ 8900 V. The applied sample voltage is ramped over the desired range, while the ESA voltage and energy window position are fixed. Since the total energy of the ions allowed into the mass spectrometer has been fixed by the ESA and the energy window, altering the extraction potential allows ions with different initial kinetic energies to be passed into the mass spectrometer. This allows the isolation of ions produced from different collision events.

The energy window position was manually set by the operator to give the highest count rate when the sample voltage was at 9000 V. The most abundant ions have low "initial kinetic energies", that is, the most common result is ions leaving with just enough energy to escape the (unknown) surface binding energy and the rest of their energy

resulting from the 9000 V on the sample. When the voltage is decreased to 8980 V, one might expect the secondary ion signal to decrease to zero because only secondary ions with 9000 eV of total energy can pass through the ESA and the energy slit. The secondary ion signal is indeed reduced, but certainly non-zero. The collision cascade from each primary beam impact will occasionally result in the ejection of ions from the sample with enough energy to make up for the low sample potential. The continued decrease in secondary ion intensity as the sample potential is decreased to 8900 V shows that the probability of these collisions of surface atoms generating secondary ions decreases with the need for higher initial kinetic energies.

In contrast, when the sample voltage is increased to 9010 or 9020 V, there is a dramatic decrease in secondary ion intensity. Any ions that are detected with negative initial kinetic energies must represent either an ion that lost energy (perhaps through a collision on the way out of the surface) or an atom that was ionized via a collision above the sample surface, and thus did not experience the full acceleration potential.

Energy spectrum analyses. One of the first analyses I was trained to perform on the ASU Cameca IMS-6f was collecting an energy spectrum. An analytical session following my training involved the study of an ilmenite megacryst from the Frank Smith mine in South Africa. The ilmenite megacryst was analyzed at a mass resolving power of $M/\Delta M$ ~3000 (see Appendix C) with a negative primary ion beam of oxygen (O^-). The sample was held at 9 kV. The energy spectra of several elements measured during this analytical session are shown in Figure 2.1.2.

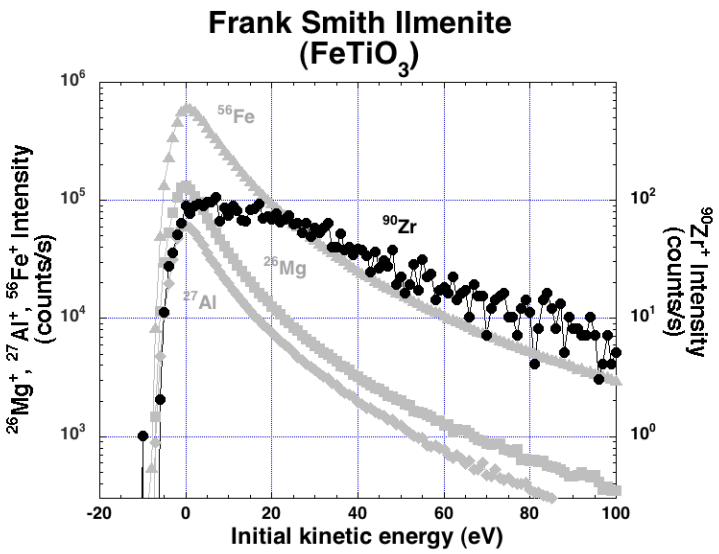

Figure 2.1.2. Energy spectrum of $^{26}Mg^+$, $^{27}Al^+$, $^{56}Fe^+$, and $^{90}Zr^+$. As in Figure 2.1.1, the initial kinetic energies of the secondary ions are shown *vs* intensities of $^{26}Mg^+$, $^{27}Al^+$, and $^{56}Fe^+$ (Y-axis on left) or $^{90}Zr^+$ (Y-axis on right).

A stark difference was noted between the peak shapes of elements like $^{26}Mg^+$, $^{56}Fe^+$, and $^{27}Al^+$ compared to the peak shape of $^{90}Zr^+$ (Fig. 2.1.2). The spectrum of $^{90}Zr^+$ not only shows a peak intensity at a higher energy, but the intense low-energy signal observed for Mg, Al, and Fe are missing for Zr. The peak shape ("missing" low-energy secondary ions) led to the investigation of $^{90}Zr^+$ as an indicator of sample fO_2 following on a study by Williams and Hervig (2000).

In their study, Williams and Hervig gathered energy spectra of $^{238}U^+$ from U metal being sputtered with an Ar beam in the presence of an oxygen backfill. The energy spectrum of $^{238}U^+$ and $^{238}U^{16}O^+$ at varying oxygen backfill pressures are shown in Figure 2.1.3A and 2.1.3B.

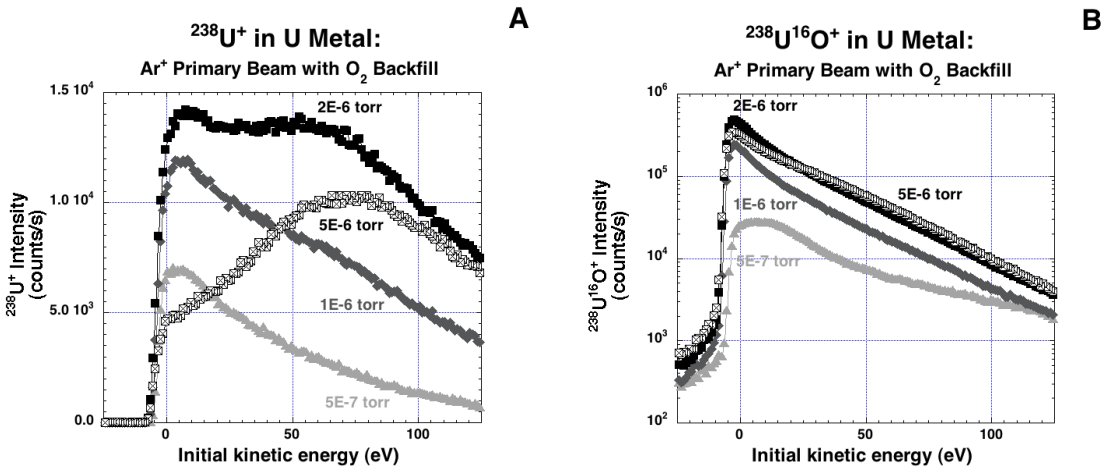

Figure 2.1.3. Energy spectra from uranium metal. The spectra were obtained at varying oxygen backfill pressures. (A) Energy spectrum of $^{238}U^+$ from uranium metal sputtered with an Ar^+ primary beam. (B) Energy spectrum of $^{238}U^{16}O^+$ from uranium metal sputtered with an Ar^+ primary beam (replotted from Williams & Hervig, 2000).

Figure 2.1.3 shows the dramatic change in the shape of the U^+ energy spectrum as the oxygen partial pressure is increased (via oxygen bleed valve). At the lowest pressure ($5e^{-7}$ torr), the spectrum appears normal (i.e., similar to Al, Mg, and Fe in Figure 2.1.2). As the oxygen pressure is increased, the low energy ions (around 0 eV) steadily increase. Around $2e^{-6}$ torr there is a significant enhancement of the high-energy ion signal and at the highest pressure ($5e^{-6}$ torr) the low energy ions essentially disappear from the energy spectrum. The spectrum strongly suggests that the normal oxygen enhancement of the U^+ signal is counteracted by some process which depleted the low energy ion flux. Williams and Hervig suggest that there is a reaction between the low energy U^+ ions and oxygen. The possible reactions suggested are shown in equation 2.1 and 2.2.

$$\mathbf{U^+ + O^- = UO^+ + e^-} \qquad \mathbf{(2.1)}$$

$$\mathbf{U^+ + O = UO^+} \qquad \mathbf{(2.2)}$$

The Williams and Hervig study shows that the formation of the oxide relates to the oxygen present in the surface of the sample during the energy spectrum analysis. This study also reveals a possible relation between the energy spectrum and oxygen activity of uranium.

In a similar study by Morgan and Werner (1977), a polycrystalline U sample containing several trace elements (Al, Si, Cr, Mn, Fe, Ni, Co, Cu, Zr, and Mo) was analyzed with a O_2^+ beam while oxygen gas was deliberately introduced into the chamber (via leak valve). Several changes in the positive secondary ion intensities by oxygen introduction are shown in Figure 2.1.4.

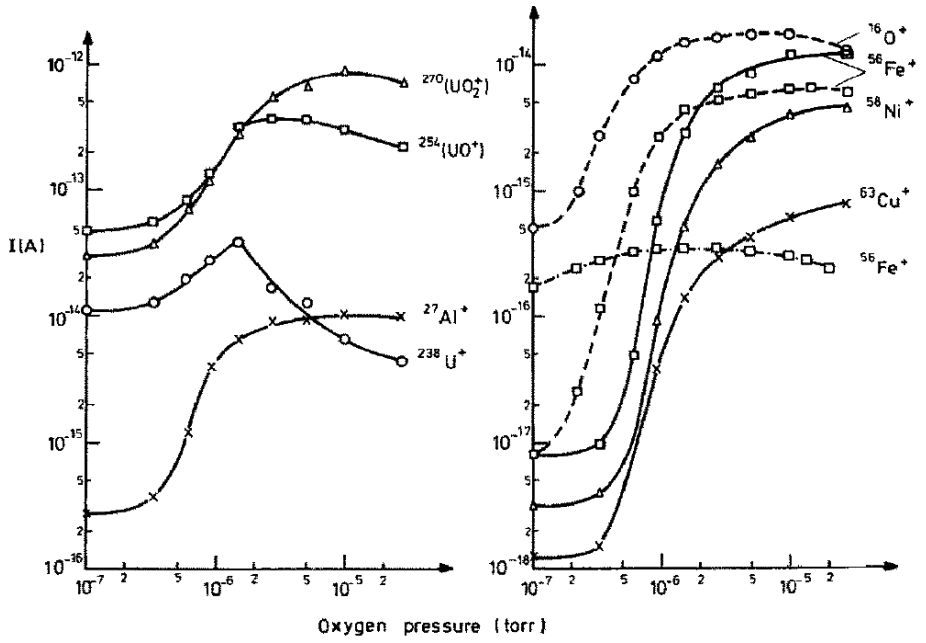

Figure 2.1.4. Secondary ion currents from 6 keV O_2^+ bombardment of uranium matrix versus nominal residual oxygen pressure (copied from Morgan & Werner, 1977).

The plots above show the peak secondary ion currents (i.e. intensities) of various elements sputtered from the sample at varying oxygen pressure. There appears to be a

correlation between the secondary ion intensity and the amount of oxygen present on the sample surface while sputtering. Morgan and Werner (1977) showed that increasing oxygen availability leads to increases in the emission of oxygen-enriched molecular secondary ions along with simultaneous decrease in the emission of oxygen-deficient molecular ions, i.e. the former molecular ions seem to be produced at the expense of the latter (Morgan &Werner, 1977). This study shows that energy spectra of some elements sputtered from metals change as a function of the amount of O coverage.

2.1.3. Analytical Methods. Following the work of Williams and Hervig (2000) and Morgan and Werner (1977), SIMS measurements of the secondary ion energy distribution of elements and oxides were conducted over the course of this study. Since this thesis explores the secondary ion energy distributions of several elements and oxides in a variety of materials, the analytical conditions for each analysis vary. In this section, I present a description of the instrumental set-up, calibration, and analytical methods used for the analyses discussed in this paper.

Instrumental calibration (for high resolution). Following the initial Frank Smith ilmenite analysis (Figure 2.1.2), the duoplasmatron was re-plumbed to generate an $^{40}Ar^{+}$ ion beam. The conditions for using this species included accelerating Ar^{+} ions to +12.5 keV energies. The primary beam was aligned such that the highest possible beam current (500 nA-1 μA) could be centered and focused in a maximum image field diameter of 250 μm. The primary ion beam current was then reduced to ~50 nA and the beam was then centered and focused in a 75 μm image field. The secondary ions were focused and

aligned using an aluminum-copper grid with squares ~25 μm^2. The entrance slit to the mass spectrometer was closed down so that the exit slit may be centered and aligned. Before the entrance and exit slits may be closed down for high resolution conditions, the secondary ion crossover must first be centered and aligned using the projector and spectrometer lens (and associated deflector sets). When the mass resolution was shown to be ~4000 (by studying the width of a peak at 10% of its height) we proceeded with analyses.

Semi-pure metal analyses. Before analyzing semi-pure metals, it is important to ensure the sample being analyzed (foil, metal, or otherwise) is completely flat in the sample holder. For foil samples like zirconium, niobium, and molybdenum, the foil was cut into a small square (~0.5 in^2) and placed into a 4-hole mount. The foil is secured with a small spring and a backing plate that is held in place with set screws in the sample mount holder.

Once the sample is loaded into the instrument, the instrument is further calibrated. The sample height is adjusted to focus the camera image of the sample surface, the magnet is adjusted for the mass of the metal accordingly (e.g., ^{90}Zr, ^{93}Nb, ^{98}Mo, etc.) and the ion image is centered and focused. For the semi-pure metal analyses, high resolution conditions are not necessary because the only mass interference we will see during these analyses are diatomic molecules of the metal, or oxides. It is, however, important that the energy window be shut down so that the energy spectra of M^+ has a full-width at half maximum value of ~10 eV. This is measured by taking energy spectra of the foil and

adjusting the energy window accordingly. Many energy spectra may be taken during this period to ensure that the operator has achieved the desired bandpass (of ~10 eV).

When analyzing semi-pure metals, it is important to ensure the metal is as clean and free from surface contamination as possible before beginning the analysis. To achieve this, the primary ion beam current is set to ~50 nA-1 μA with raster of 250 x 250 μm^2. The primary ion beam is then rastered over the surface of the sample for 20-40 minutes before the initial analysis is performed.

Once a sputter-cleaned surface is created, the beam current is adjusted to 10-50 nA and the analysis is designed so that the primary ion beam is rastered over an area of 250 x 250 μm^2, the maximum image field is 75 μm and the second field aperture is used to analyze a total diameter of 30 μm. The sample energy is varied over a range of -30 eV to +100 eV (most commonly between -20 eV to +60 eV which relates to a sample voltage of 4940 eV-5020 eV) with a 1 second integration time per 1 eV step. Because the secondary ion intensity increases as oxygen is added to the sample, it is important to keep the peak signals at ~10,000 counts/second on the bare metal so that the secondary ion detector is not be switched from the electron multiplier to the faraday cup (at intensities $>1x10^6$ counts/second) when the oxygen backfill is used. This did occur on occasion, requiring a repeat of the set of analyses with the energy window closed slightly (after characterization) to decrease the maximum counts at the base pressure.

After measuring energy spectra of the M^+, MO^+, and MO_2^+ ions at the base analysis pressure, the oxygen bleed valve was carefully opened while the analysis chamber pressure gauge is monitored. It is important to note that the actual pressure at the sample surface is somewhat higher since the gas was introduced directly at the target via

a closely-positioned capillary. Morgan and Werner (1977) pointed out that all pressure readings given, except the starting pressure, are liable to be underestimated. The ion currents and pO_2 backfill pressures were noted when steady state values had been reached while actively sputtering the sample surface.

Geologic sample analyses. Before analyzing geologic samples like ilmenite ($FeTi_2O_3$), baddeleyite (ZrO_2), or rutile (TiO_2), it is important to ensure the sample being analyzed is completely flat in the sample holder. All geologic samples analyzed are pre-made thin sections, polished megacrysts mounted in epoxy, or are pre-polished rock slabs suitable for a 1" diameter sample holder. All geologic samples are also coated with a thin (~20-30 μm thick) layer of gold to create a conducting layer that prevents sample charging in the event that the conducting phases of interest were surrounded by insulating silicate phases.

Once the sample is loaded into the instrument, the instrument is further calibrated. The sample height is adjusted to focus the camera image on the sample surface, and the beam is moved to a rough spot on the sample to adjust/tune the beam size and position and tune the magnet accordingly. On a clean area, a crystal of ilmenite (nominally $FeTiO_3$) was sputtered with Ar^+ until the secondary ion signal reached steady state (~ 50 nA primary current, 50 x 50 μm raster, 30 μm diameter analyzed area). Following Gnaser and Hutcheon (1987), a complex molecular ion ($^{48}Ti^{16}O_2^+$) was used to determine the size of the energy bandpass because such molecular ions have narrow energy distributions compared to typical elemental ions. An example is shown in Figure 2.1.5.

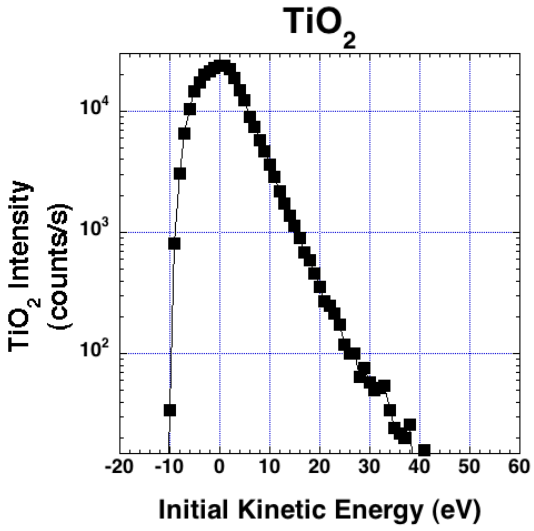

Figure 2.1.5. Energy spectrum of TiO_2 measured in Frank Smith ilmenite. The spectrum was taken as a calibration measurement of the energy window. This spectrum is representative of an energy window measured at ~10.7 eV.

To set the mass resolving power, a high-resolution mass scan of an elemental ion of interest (usually Zr or Nb when examining ilmenite) is obtained. The width of the entrance and exit slits and the projection and spectrometer lenses are adjusted to achieve flat-topped peaks and sufficient separation between the elemental and interfering molecular ions. A high-resolution mass scan of $^{93}Nb^{+}$ in Frank Smith ilmenite is shown in Figure 2.1.6.

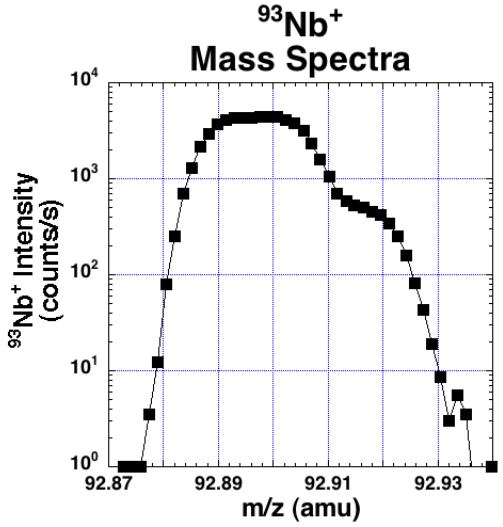

Figure 2.1.6. High-resolution mass scan of $^{93}Nb^+$ in Frank Smith ilmenite.

The high-resolution mass scan measurement in Figure 2.1.6 was taken as a calibration measurement of the mass resolving power. The Nb signal is the more abundant peak on the left while the smaller shoulder on the right is an interfering molecular ion with a similar atomic weight as $^{93}Nb^+$. Similar spectra obtained on other elements (e.g., ^{26}Mg) showed that these conditions represent a mass resolving power ($M/\Delta M$) ~4000 (see Appendix C).

Finally, the beam current is adjusted to values between 35-60 nA and the analysis recipe is written so that the beam is rastered over an area of 50 x 50 μm^2, the maximum image field was 75 µm and the second field aperture was used to collect ions from a circular area 30 µm in diameter. The sample voltage is most commonly varied in 1 V increments from 5020 to 4940 V with an integration time between 0.5-10 seconds per step (depending on the secondary ion signal strength).

Once the analysis recipe is written and calibrated, energy spectra of various elements and oxide ions are measured. For analysis of geologic samples, the energy spectrum was not measured over a range of oxygen backfill pressures.

2.2 RESULTS

Over the course of this study, many energy spectrum analyses were performed on a variety of materials in pursuit of identifying a relationship between the energy distribution of secondary ions and the amount of oxygen present in a sample. To explore this relationship, a number of different samples, analytical methods, and data analysis methods were employed. The following section explores the results of the various investigations performed throughout this project. To obtain baseline information on the behavior of different elements as a function of oxygen coverage, some polycrystalline metal foils were studied. In these cases, the signal was abundant, the matrix was a conductor, and there was little restriction on the amount of material available for testing. After describing these results, similar energy spectra were obtained on natural samples. They are described, and the differences between the spectra on metals and oxides are interpreted in Section 2.3.

2.2.1 Oxide vs. Element. Like Williams and Hervig (2000), and Morgan and Werner (1977), I have conducted several investigations to study the relationship between the secondary ion distribution of various elements and their oxides.

Zirconium. Similar to the 2000 study by Williams and Hervig, zirconium foil was analyzed with a primary ion beam of $^{40}Ar^{+}$ over a range of oxygen backfill pressures

while energy spectrum of the M^+ and MO^+ ions where measured. The energy spectrum of $^{90}Zr^+$ and $^{90}Zr^{16}O^+$ at varying oxygen backfill pressures are shown in Figure 2.1.7.

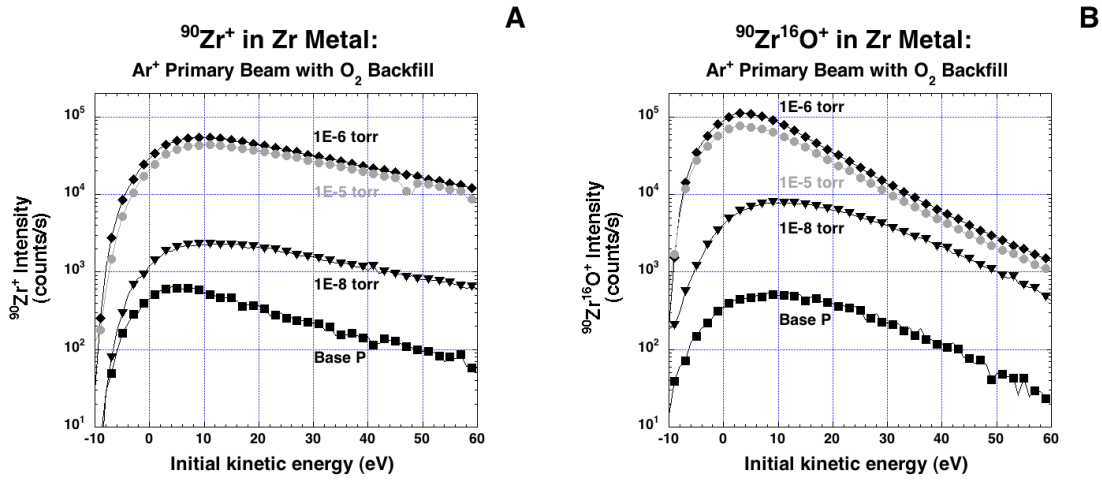

Figure 2.2.1. Energy spectra measured on zirconium metal. The spectra were obtained at varying oxygen backfill pressures. (A) Energy spectrum of $^{90}Zr^+$ from zirconium metal sputtered with an Ar^+ primary beam. (B) Energy spectrum of $^{90}Zr^{16}O^+$ from zirconium metal sputtered with an Ar^+ primary beam.

The energy spectrum of $^{90}Zr^+$ at base analysis pressures appears normal (when compared with Figure 2.1.1 and 2.1.2). That is, it shows a narrow low-energy peak and a high-energy tail. As oxygen is added to the sample surface during sputtering, the intensity of the elemental ion increases, and the position of the maximum intensity appears to shift to higher energies. The $^{90}Zr^+$ spectrum peaks become increasingly wider and the counts increase up to backfill pressures of ~$1e^{-6}$ torr where they plateau and then begin to drop. As oxygen is added to the sample surface, the peaks of the $^{90}Zr^{16}O^+$ spectrum increase up until ~10^{-6} torr where the peak counts begin to drop, similar to the spectrum of $^{90}Zr^+$. The energy spectra in Figure 2.2.1 shows secondary ion energy distribution behavior similar to that seen by Morgan and Werner (1977); increasing oxygen availability causes the oxygen-bearing molecular ions to form at the expense of the elemental species.

Energy spectra of $^{93}Nb^{+}$ in ilmenite showed similar secondary ion distribution behavior as $^{90}Zr^{+}$, so semi-pure niobium metal was analyzed next.

Niobium. Energy spectra analyses were performed on niobium foil with a primary beam of $^{40}Ar^{+}$ over a range of oxygen backfill pressures while energy spectrum of the M^{+} and MO^{+} ions where measured. The energy spectrum of $^{93}Nb^{+}$ and $^{93}Nb^{16}O^{+}$ at varying oxygen backfill pressures are shown in Figure 2.2.2.

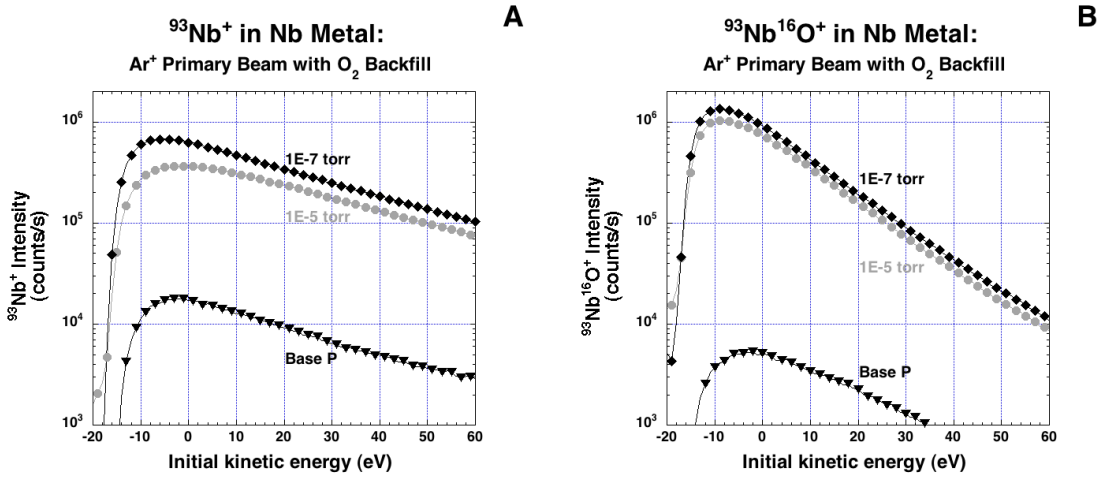

Figure 2.2.2. Energy spectra measured on niobium metal. The spectra were obtained at varying oxygen backfill pressures. (A) Energy spectrum of $^{93}Nb^{+}$ from niobium metal sputtered with an Ar^{+} primary beam. (B) Energy spectrum of $^{93}Nb^{16}O^{+}$ from niobium metal sputtered with an Ar^{+} primary beam.

The energy spectrum of $^{93}Nb^{+}$, similarly to the energy spectrum of $^{90}Zr^{+}$, appears normal at base pressures and shows a narrow low-energy peak and a high-energy tail. As anticipated, the peak appears to shift to higher energies (e.g., from $1e^{-7}$ to $1e^{-5}$ torr) while it simultaneously broadens as oxygen is added. The $^{93}Nb^{+}$ spectrum peaks become increasingly wider and the counts increase up to ~$1e^{-7}$ torr before counts begin to drop (not all spectra shown). As oxygen is added to the sample surface, the peak intensity of

the $^{193}Nb^{16}O^{+}$ ion increase up until ~$1e^{-7}$ torr where the peak counts begin to drop, similar to the $^{93}Nb^{+}$ spectra. Secondary ions of niobium appear to behave similarly to Zr.

Semi-pure metals. The analyses of zirconium and niobium for the purpose of studying the relationship between the secondary ion energy distribution and the amount of oxygen present in the sample surface were conducted because it was observed that the shapes of the Zr and Nb spectra in natural ilmenites were different than most other elements (Figure 2.1.2). Similar spectra on other semi-pure metals were obtained by Dr. Richard Hervig. These analyses were conducted to determine if other elements might show "non-normal" energy spectra as a function of oxygen coverage. The results were presented in a talk at the Goldschmidt Conference in August, 2018 (Hervig, Dillon, & Williams, 2018). In Figures 2.2.3-2.2.5 the energy spectrum of M^{+} and MO^{+} in three semi-pure metals at varying oxygen backfill pressures are shown.

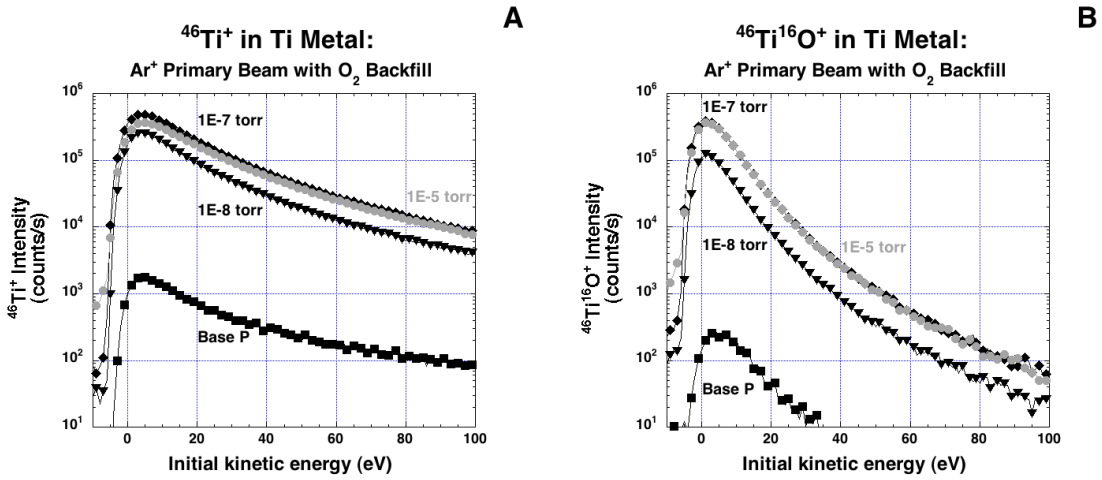

Figure 2.2.3. Energy spectra measured on titanium metal. The spectra were obtained at varying oxygen backfill pressures. (A) Energy spectra of $^{46}Ti^{+}$ from titanium metal sputtered with an Ar^{+} primary beam. (B) Energy spectra of $^{46}Ti^{16}O^{+}$ from titanium metal sputtered with an Ar^{+} primary beam.

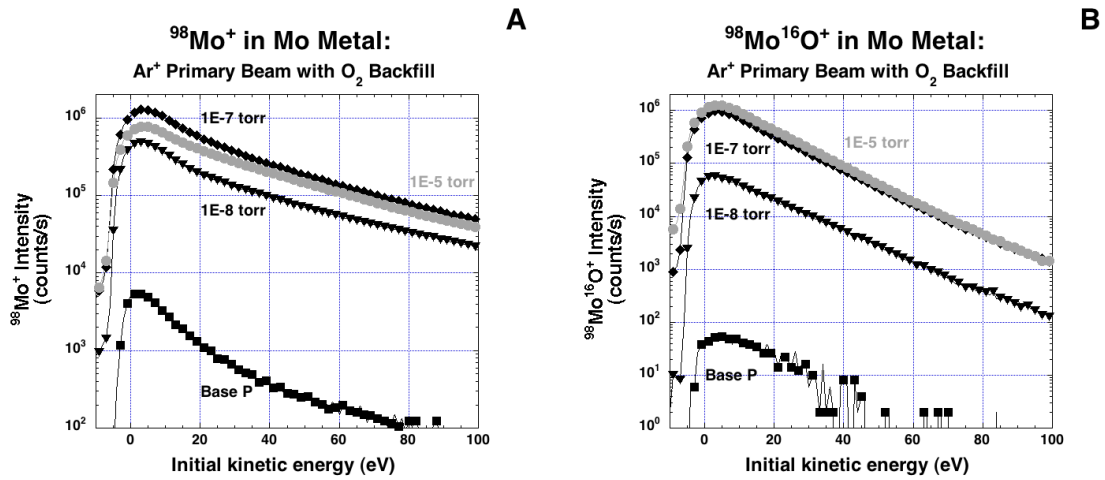

Figure 2.2.4. Energy spectra measured on molybdenum metal. The spectra were obtained at varying oxygen backfill pressures. (A) Energy spectrum of $^{98}Mo^+$ from molybdenum metal sputtered with an Ar^+ primary beam. (B) Energy spectrum of $^{98}Mo^{16}O^+$ from molybdenum metal sputtered with an Ar^+ primary beam.

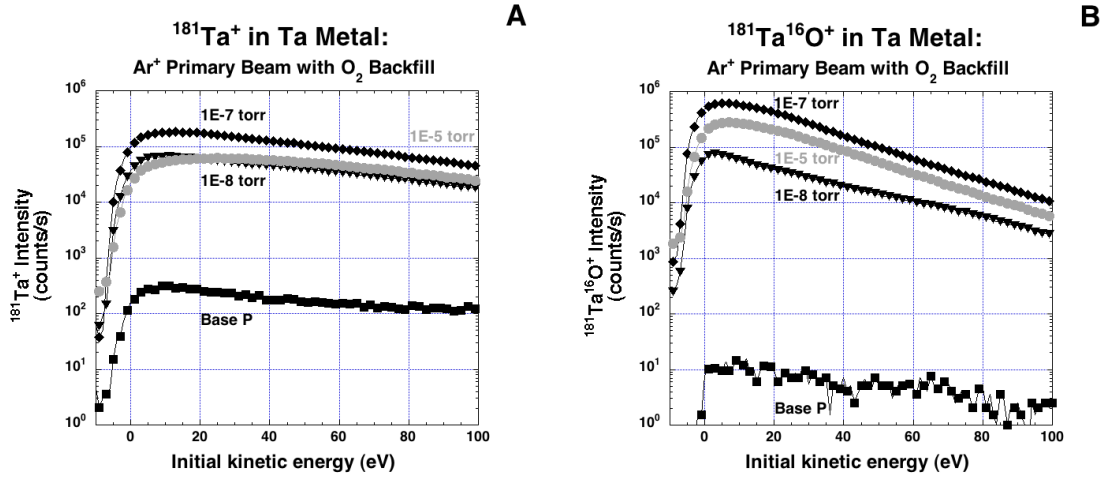

Figure 2.2.5. Energy spectra measured on tantalum metal. The spectra were obtained at varying oxygen backfill pressures. (A) Energy spectra of $^{181}Ta^+$ from tantalum metal sputtered with an Ar^+ primary beam. (B) Energy spectra of $^{181}Ta^{16}O^+$ from tantalum metal sputtered with an Ar^+ primary beam.

2.3 DISCUSSION

Semi-pure metals. The purpose of analyzing these semi-pure metals is to identify elements that may reflect changing shapes of their energy spectra as a function of oxygen content. A metal that produces a variety of energy spectra over a wide range of oxygen pressures would be an ideal sample to study. Zirconium and niobium analyses show that oxygen pressures over a range of ~2 orders of magnitude result in significant changes in the secondary ion intensity of energy spectra along with the peak shape. There appears to be some oxygen backfill pressure at which the secondary ion signals begin to drop for the M^+ and MO^+ ions (>1e^{-6} torr). Due to the increase in MO^+ ions, it seemed important to examine how the ratio of oxide to elemental ions changed with increasing oxygen coverage. It is anticipated that this ratio might be a quantitative marker of oxygen activity in the crater. The MO^+/M^+ ion ratios of the metal analyses are shown in Figure 2.3.1.

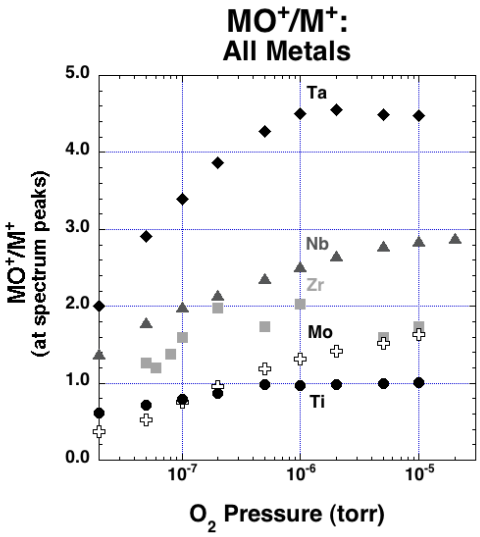

Figure 2.3.1. Secondary ion current ratios of MO^+/M^+ vs. nominal residual oxygen pressure. The ratio of MO^+/M^+ was calculated using the peak intensities for each species.

Figure 2.3.1 shows variable correlations between the amount of oxygen present at the sample surface during sputtering and the MO^+/M^+ ratio. In particular, Ta, Nb, and Mo show the strongest correlations. The MO^+/M^+ ratios of sputtered Ti metal appear to increase only slightly, reaching a constant value just below a backfill pressure of $1e^{-6}$ torr. The Zr metal shows MO^+/M^+ ratios that vary but are scattered. While the Ta metal shows the largest change in MO^+/M^+ from ~$1e^{-8}$ to $1e^{-6}$ torr, the ratio peaks around $1e^{-6}$ torr. Overall, there are inconsistent changes in the oxide/element ion ratios. Thus, it would appear that using them to predict sample oxygen activity would not (at present) be a good approach.

Geologic samples. Energy spectra of the M^+ and MO^+ ions within several geologic samples were measured at base analysis pressures. No oxygen was added to the sample surface via oxygen backfill. The analyses of geologic samples were conducted to correlate the energy spectrum peak shape or MO^+/M^+ ratio of the peak values to a measured energy spectrum from a semi-pure metal with a known oxygen backfill pressure. If the results of these analyses compared with the results of semi-pure metal analyses indicate any kind of relationship, it might be possible to predict the sample fO_2 of natural oxides. If calibrated, there is a potential to directly measure the oxygen fugacity of a natural phase by SIMS microanalysis. As an example, the energy spectra of clean and oxidized Zr metal versus the energy spectrum of crystalline baddeleyite (ZrO_2) were compared; these spectra are shown in Figure 2.3.2.

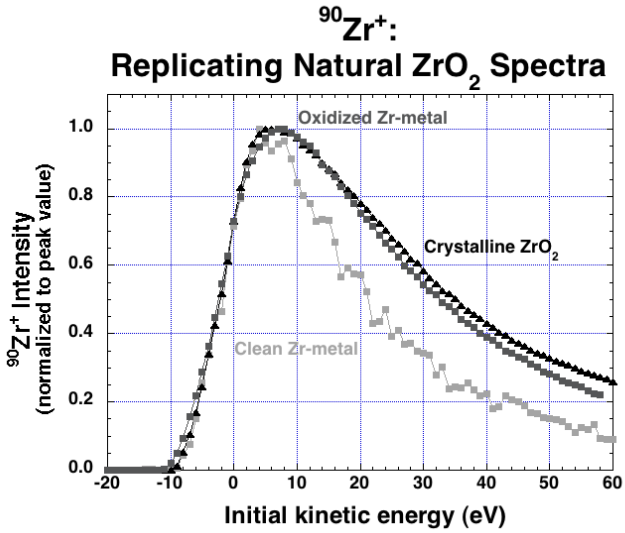

Figure 2.3.2. Energy spectra for $^{90}Zr^+$ in clean and oxidized zirconium metal and in crystalline baddeleyite (ZrO_2). The backfill pressure of the "clean" Zr metal was $<8e^{-8}$ torr while the backfill pressure of the oxidized Zr metal was $\sim 1e^{-6}$ torr. The peak intensities are normalized to 1 to better compare the peak widths.

During this analytical session, the crystalline baddeleyite (ZrO_2) was analyzed at base vacuum pressures before analyzing the zirconium metal. In this analytical session, energy spectra of $^{90}Zr^+$ were taken at varying oxygen backfill pressures. The energy spectrum for the "clean" zirconium metal was measured at a backfill pressure $\sim 1e^{-8}$ torr while the oxidized zirconium metal energy spectrum was measured at a backfill pressure $\sim 1e^{-6}$ torr. An attempt was made to replicate the energy spectrum of the crystalline baddeleyite (ZrO_2), but matching the spectra was not exactly achieved. Similar energy spectra were obtained on ilmenite ($FeTiO_3$) but any variations in the peak shape and intensity between different ilmenite crystals was not resolvable (see Fig. 2.3.6 below).

2.3.1 Full-width at half maximum. Once no consistent relationship between the MO^+/M^+ ratios for the energy spectra could be found, investigation into the peak shape

began. To further investigate the change in the peak shapes of energy spectrum, the M^+ and MO^+ spectra of the semi-pure metals were plotted such that the peak signals are normalized to 1. The semi-pure metal energy spectra are compared against each other at a particular oxygen backfill pressure ($1e^{-6}$ torr) in Figure 2.3.3.

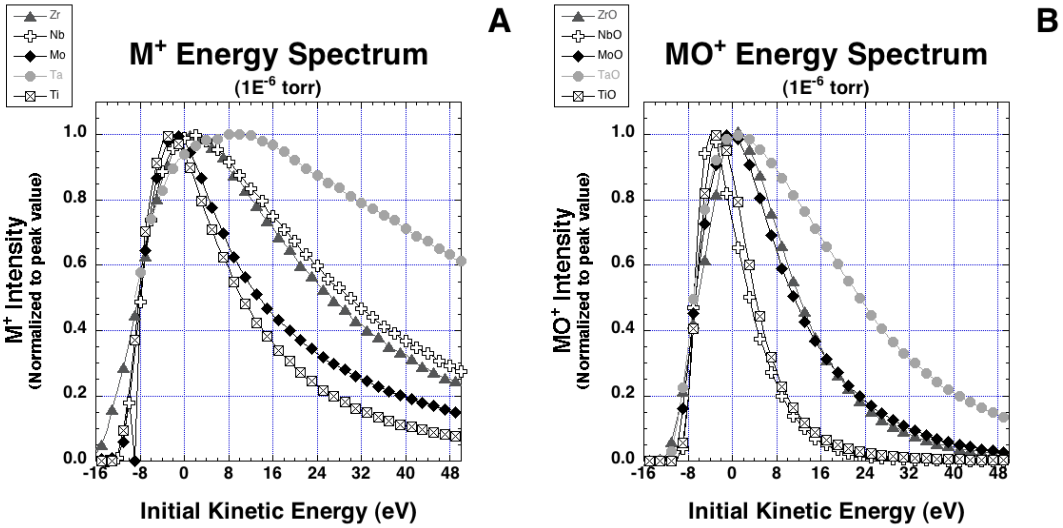

Figure 2.3.3. Energy spectra determined on semi-pure metals. The spectra shown were obtained at an oxygen backfill pressure of 10^{-6} torr. (A) Energy spectra of M^+ from semi-pure metal sputtered with an Ar^+ primary beam. (B) Energy spectra of MO^+ from semi-pure metal sputtered with an Ar^+ primary beam. The peak intensities are normalized to 1 to better compare the peak widths. The spectra were also shifted so the low energy side of each spectra is aligned.

It is apparent that the elemental energy spectra display very different shapes. Ti and Mo display relatively narrow peaks while Zr, Nb, and Ta show much wider peaks. The oxide ions also show varying widths but the peak energies do not match up with each other in these analyses (at a backfill pressure of $1e^{-6}$ torr). To put a number on the peak shape, the full-width at half maximum values were calculated at each oxygen backfill pressure and shown in Figure 2.3.4.

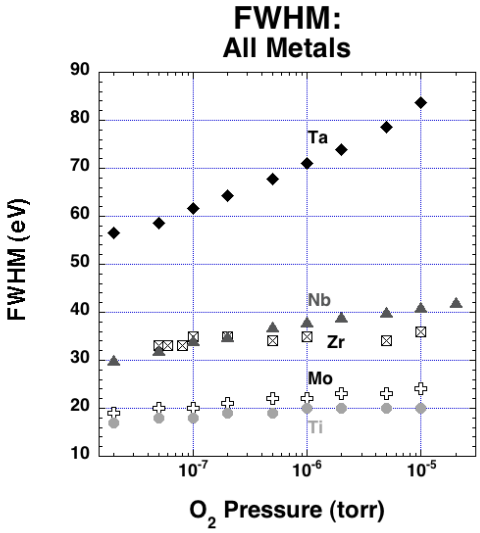

Figure 2.3.4. Calculated FWHM values of energy spectra of the elemental ions sputtered from semi-pure metals as a function of varying oxygen backfill pressures as represented by the vacuum gauge in the analysis chamber (underestimated compared to the actual O_2 partial pressure at the sputtering site).

The calculated FWHM values for the spectra of semi-pure metals increase with increasing oxygen backfill. Although this relationship does not exist at very low pressures ($<2e^{-8}$ torr), it is clear at higher pressures; particularly for Ta and Nb and to a lesser extent for Mo. The Nb and Ta spectra widen with increasing oxygen while the Ti, Mo, and Zr spectral shapes are nearly constant with increasing oxygen.

2.3.2 Comparison of results

Energy spectra. The energy spectra of $^{90}Zr^{+}$ and $^{93}Nb^{+}$ gathered on natural ilmenites were compared on several occasions to determine a relationship between the shape of the spectra and the sample's inferred fO_2 (i.e., oxidized or reduced relative to the environment in which they formed). Analytical sessions in which the highest

secondary ion intensities and the most reproducible FWHM were obtained for each sample are shown below in Figures 2.3.5 and 2.3.6.

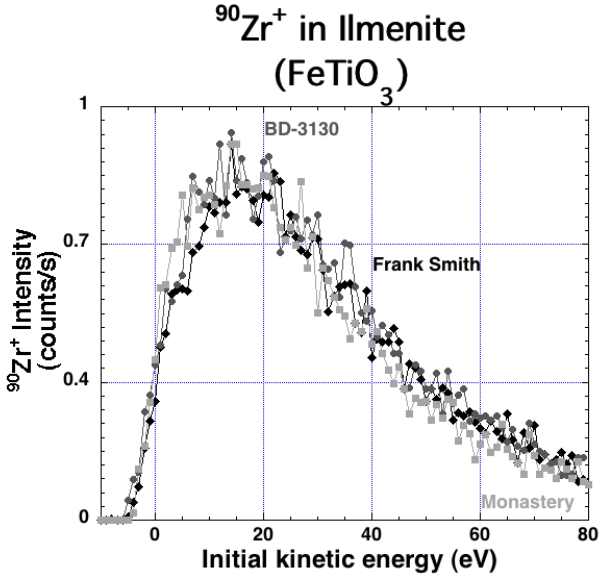

Figure 2.3.5. Energy spectra of $^{90}Zr^+$ in BD-3130, Frank Smith, and Monastery ilmenites. The peak intensities are normalized to 1 to better compare the peak widths.

The spectra shown in Figure 2.3.5 appear to lay on top of each other, suggesting similar FWHM values for each ilmenite. The spectra are also fairly "noisy" because of the low secondary ion intensities. Juvinas ilmenite is not displayed in Figure 2.3.5 because the Zr^+ intensities were even lower, and the peak widths were difficult to calculate due to "noisy" spectra.

Upon examination of the results from several analytical sessions, it was concluded that $^{90}Zr^+$ should not be used for this analytical technique because the spectra do not vary over the range of fO_2 exhibited by our natural samples.

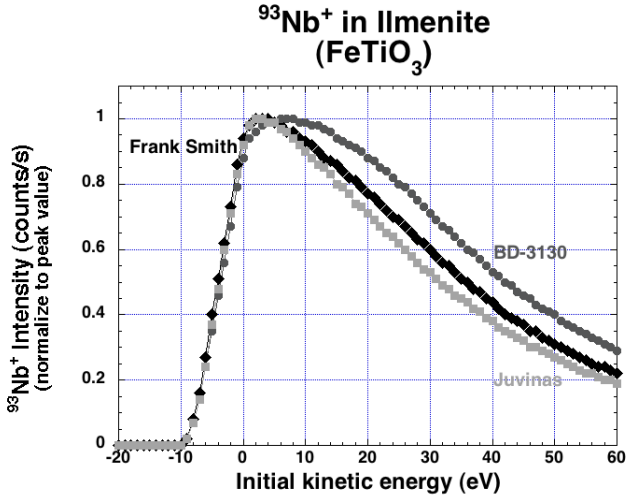

Figure 2.3.6. Energy spectra of $^{93}Nb^{+}$ in BD-3130, Frank Smith, and Juvinas ilmenites. The peak intensities are normalized to 1 to better compare the peak widths.

Unlike Figure 2.3.5, Figure 2.3.6 shows a visible difference between the peak widths of these ilmenites. The spectra are smooth and showed high secondary ion signals in these ilmenites that were reproducible between analytical sessions. The smoothness results from the relatively high Nb contents and from using long integration times (10 seconds) during each voltage step when obtaining these spectra. The variation in the spectral shapes suggests that Nb is likely a better candidate for testing the effect of sample fO_2 on the peak shape of energy spectrum in ilmenites. Monastery ilmenite is not displayed in Figure 2.3.6 because the secondary ion intensities were very low for Nb and the peak widths were difficult to calculate due to "noisy" spectra. Due to the low Nb contents, Monastery ilmenite also produced the least reproducible FWHM data among all the samples analyzed in this study. These spectra show a shift in the peak energy to higher or lower intensities values to the sample's inferred fO_2 (i.e., more oxidized or reduced relative to other samples). The spectrum obtained on Juvinas, our most reduced

ilmenite, is both narrow and shows a peak shifted to lower kinetic energies (i.e., left) while the spectrum of BD-3130, our most oxidized sample, is wider and the peak is shifted to higher energies (i.e., right). Based on the 2000 study by Williams and Hervig, shifting peak intensities to higher energies would suggest increasing relative fO_2 of these samples

Electron probe microanalyses. To better understand the relationship between the peak width of $^{93}Nb^{+}$ energy spectra and the sample fO_2, the natural ilmenites were analyzed via electron microprobe (i.e., EMPA) to quantify the amount of hematite, geikelite, and ilmenite within each sample. These analyses were used to calculate the Fe^{3+}/Fe^{2+} ratio, the $Fe^{3+}/\sum Fe$ ratio, and the molar amounts of the end-members hematite ($Fe^{3+}{}_2O_3$), geikelite ($MgTiO_3$), and ilmenite ($FeTiO_3$) for each sample.

The Electron Probe Microanalyzer (EMPA) used for these analyses is JEOL's JXA-8530F Hyperprobe. This instrument was used primarily for the identification of constituent elements and their distribution in the ilmenite samples analyzed for this study. Analyses are performed in this instrument by illuminating the surface with a finely focused electron beam and measuring the intensities of characteristic x-rays emitted from the samples. This technique is non-destructive, and analyses could be obtained very close to some of the SIMS craters made in the ilmenites. The data from the EMPA analyses of the various ilmenites used throughout this study are presented below in table 2.3.7.

Table 2.3.7

Electron Microprobe Data and Nb FWHM for Ilmenite Samples

Sample	Calculated FWHM	Fe^{3+}/Fe^{2+}	$Fe^{3+}/\sum Fe$	Ilmenite (%)	Hematite (%)	Geikelite (%)
BD-3130	45 ± 1eV	0.4581	0.3142	66.18	15.14	18.68
Frank Smith	40 ± 1eV	0.3327	0.2497	55.60	9.25	35.15
Monastery	40 ± 3eV	0.2626	0.2080	55.86	7.73	33.4
Juvinas	35 ± 1eV	0.0000	0.0000	96.77	0.00	3.23

The implied differences between these ilmenites is represented in table 2.3.7. The eucrite meteorite Juvinas contains Fe-metal and is assumed to be in the vicinity of the Iron-Wüstite buffer (see Ch.1 section 1.3). Frank Smith ilmenite is thought to have formed from a primitive melt at about QFM while the BD-3130, the MARID sample, is from a metasomatized rock and is expected to be a bit more oxidized. Monastery ilmenite has been estimated to form at around the same conditions as Frank Smith (QFM) and they share a similar chemistry. The compositions of these ilmenites may be plotted in other ways to better visualize the differences between these samples. Figure 2.3.7 below shows the composition of each sample within the $FeTiO_3$-$MgTiO_3$-Fe_2O_3 system on a ternary diagram.

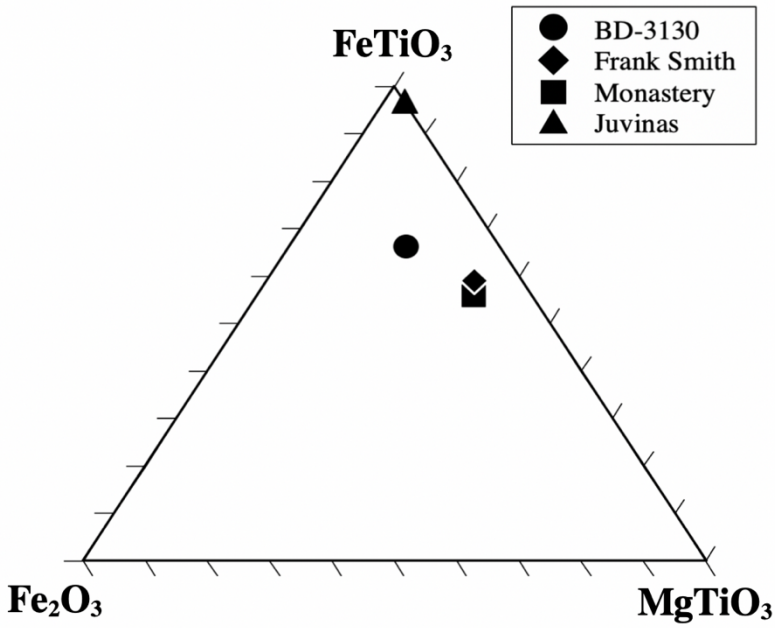

Figure 2.3.7. Ternary diagram showing the composition of ilmenite samples analyzed throughout this project (analyses from Table 2.3.7).

The ternary in Figure 2.3.7 displays the composition of these ilmenite samples relative to their ilmenite-geikelite-hematite content. BD-3130 is our most oxidized sample containing ~15% hematite; this is consistent with our hypothesis because the energy spectra peak width of BD-3130 is consistently wider than other ilmenites analyzed. Juvinas is our most reduced sample containing no ferric iron (according to the EMPA results) and the energy spectra peak width is narrower than other ilmenites. The peak width of the energy spectra of Frank Smith ilmenite sits between the peak widths of Juvinas and BD-3130.

Because we have abundant amounts of the Frank Smith ilmenite, it was used as a reference material. In each analytical session one or two fragments of Frank Smith were analyzed to ensure the FWHM was similar or the same from session to session.

Variations in the Nb FWHM on this ilmenite could be caused by the operator setting the energy window slightly differently in one session vs. another, so all ilmenite analyses were compared to the value obtained on the Frank Smith sample in each session.

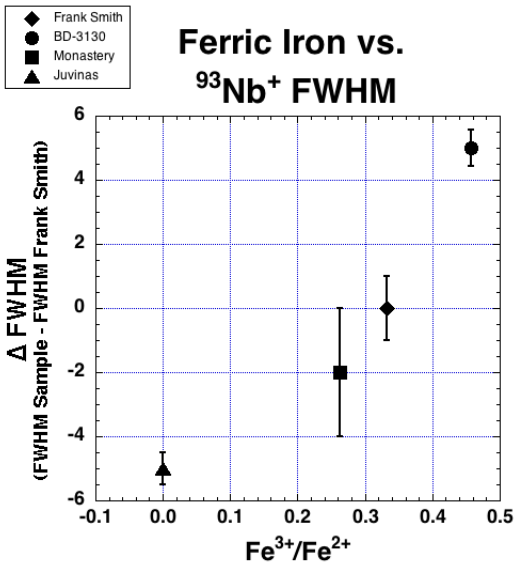

Figure 2.3.8. ΔFWM of $^{93}Nb^{+}$ vs. Fe^{3+}/Fe^{2+} in each ilmenite sample. The Δ FWHM value represents the FWHM of an ilmenite (from Figure 2.3.7) minus the FWHM of the Frank Smith ilmenite from the same analytical session. The units of the ΔFWHM in this figure are eV.

The results presented in Figure 2.3.8 show the correlation between the Nb FWHM and the ferric/ferrous ratio (from the electron probe results – see Table 2.3.7). Assuming that Juvinas is in the vicinity of the IW (iron-wüstite) buffer and Frank Smith is in the vicinity of the QFM (Quartz-Fayalite-Magnetite) buffer (roughly 5 log units higher fO_2), Figure 2.3.8 implies that a 1 eV increase in the FWHM corresponds to ~1 log unit increase in fO_2 (see Figure 1.2.2). The pronounced increase in the FWHM of the veined, metasomatized peridotite BD-3130 would suggest a much higher fO_2, but it is not known if the change in FWHM should be expected to be linear in fO_2. Clearly, studying ilmenite

crystals synthesized at known oxygen fugacities is critical to making progress in this field.

This analytical technique focuses on the empirical relation between the FWHM of the energy spectra peak of $^{93}Nb^{+}$ and inferred oxygen fugacity. The role of major and minor element compositional variations among these ilmenites has not been considered. One major compositional variable is magnesium. Mg and Ti can both have an effect on the stability of oxides, but in this study the variability of the Ti content is not as important since it is a major component in ilmenite. Based on the results presented in Figure 2.3.7 and 2.3.8, it will be important to determine (via synthesizing standards) if elements besides Fe and Ti have a large effect on the Nb energy spectra and hence the inferred fO_2 of the sample.

Possible Mechanism. Following Williams and Hervig (2000), a reaction occurring in the floor of the sputtered crater is suggested in equation 2.3.

$$\mathbf{Nb^{+} + O = NbO^{+}} \qquad \mathbf{(2.3)}$$

The suggestion is that the capture of Nb ions by oxygen occurs more readily on surfaces with higher activities of oxygen and more frequently when considering low-energy Nb ions (which are relatively low-velocity ions). Higher energy Nb ions may avoid the interactions with surface oxygen because of their high velocity. If so, this would generate energy spectra where the peak ion intensity changes to higher energies with higher oxygen coverage, or oxygen activity at the sample surface.

2.4 CONCLUSIONS

The examination of energy spectra of a range of metals shows that some elements change the shape of their spectra when the surface they originate from changes from less to more oxidized. The energy spectra for niobium sputtered from natural ilmenites are also shown to change with increased ferric iron content. While the causes of the increase in the FWHM of the niobium energy spectrum are not known for certain, it is suggested that this technique may be developed to the point where it can be used to determine changes in fO_2 of a sample from core to rim (i.e., detecting changes in conditions during crystal growth). The major uncertainties relate to the lack of samples synthesized at controlled values of fO_2 to anchor a calibration and the lack of information as to the role of other elements to influence the energy spectra shape.

CHAPTER 3

ANALYTICAL APPLICATIONS

3.1 INTRODUCTION

This chapter presents analyses of synthetic and natural oxide minerals. These data are representative of potential applications for the microanalytical technique presented in this thesis.

3.2 EXPERIMENTAL TiO_2

To test our hypothesis that energy spectra of certain sputtered ions can be related to the fO_2 at which oxide minerals formed, we acquired experimental samples of TiO_2 synthesized at a range of fO_2 at 1 atmosphere. The experiments were doped with an oxide mix containing V, Sc, Cr, Y, La, Ce, Pr, Nd, Sm, Eu, Gd, Dy, Ho, Er, Yb, Lu, Nb, and Ta (Nb and Ta concentrations ~200-800ppm).

The general method for the experiments involved slow cooling of a melt from 1500˚C to 1300˚C at 6˚C/hour and then dwelling at 1300˚C for two days. During this dwell time, TiO_2 crystals are expected to grow from the melt. The samples analyzed include two major compositions: DacTi (i.e., a dacitic composition with added titanium) and MORBTi (i.e., basaltic material with added titanium). These analyses focused on the DacTi samples because the melt was more polymerized. This increases the Nb and Ta partition coefficients, thus creating Nb-rich rutile crystals. The samples analyzed were DacTi at QFM-1 log unit fO_2, QFM, QFM+1, and DacTi in air at 1100˚C (i.e., NNO+7 or QFM+8; Frost 1991a). All experimental runs contained a TiO_2 phase.

3.2.1 Analytical Methodology. Analyses of experimental TiO_2 samples were conducted at similar conditions as the natural ilmenites discussed in Chapter 2. The mass resolving power for these analyses was M/ΔM ~3000 that was measured at $^{51}V^+$. The samples were sputtered with a primary ion beam of $^{40}Ar^+$ with ~40nA beam current. The analysis was designed so the primary ion beam was rastered over an area of 50 x 50 μm^2, the maximum image field was 75 μm and the third field aperture was used to analyze a total diameter of 15 μm. The third field aperture was used to prevent secondary ions from surrounding crystals to be measured. The experiments contained small TiO_2 crystals which were intergrown with quenched melt and silicate crystals.

The analysis recipe is also written so that the sample potential was varied from 4940-5020 V. Due to low secondary ion signals of $^{93}Nb^+$ in these samples, the integration time was adjusted accordingly. Identification of an appropriate area to study was done by moving the primary ion beam onto a grain and looking at the secondary ion images of $^{27}Al^+$, $^{28}Si^+$, and $^{48}Ti^+$. The sample and primary beam position were moved together to maximize the signal from Ti and minimize the Si signal (to minimize overlap on silicate phases).

3.2.2 Results. FWHM values calculated from the energy spectrum of niobium obtained on experimental TiO_2 samples are shown below in table 3.2.2.

Table 3.2.2

Calculated FWHM Values for Experimental TiO_2 Samples

Sample	Calculated FWHM
QFM-1	18 eV
QFM	16 eV
QFM+1	17 eV
QFM+8	21 eV

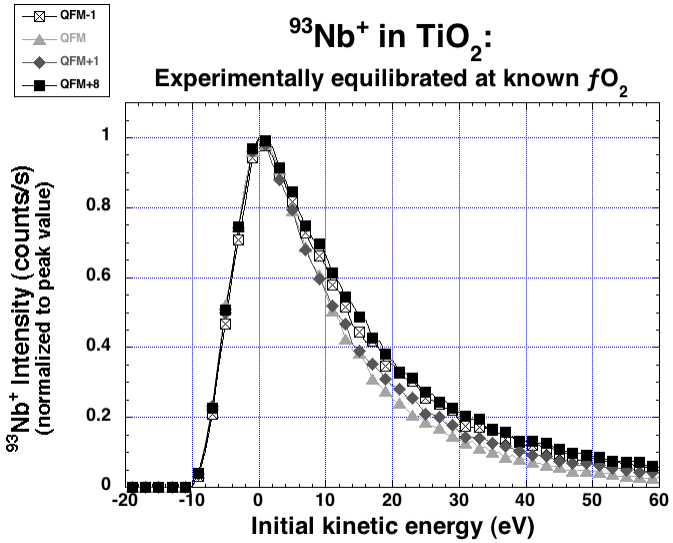

Figure 3.2.2. Energy spectra of $^{93}Nb^{+}$ in experimental TiO_2 samples equilibrated at varying fO_2 conditions. The peak intensities are normalized to 1 to better compare the peak widths.

3.2.3 Discussion. The calculated FWHM values for most of the experimental TiO_2 samples analyzed agree with the observation in Chapter 2 that increasing fO_2 is represented by increasing FWHM of the Nb energy spectrum. Considering the 1 eV uncertainty in the FWHM, sample QFM-1 is an outlier. The FWHM was calculated from the energy spectra shown in Figure 3.2.2. If this sample followed the hypothesized

FWHM trend, the FWHM would be expected to be small, perhaps ~14-15 eV. It is possible that the lack of large TiO_2 crystals in the charge resulted in this unexpected FWHM value.

Sample QFM-1 consisted of a single, small (~200 x 30 μm) crystal that included phases other than TiO_2. Secondary ion images of silicon, aluminum, magnesium, iron, and titanium were used to identify the other phase and their location in relation to the TiO_2 portion of the grain. The images in Figure 3.2.3 below became very useful when trying to find a rutile-rich location.

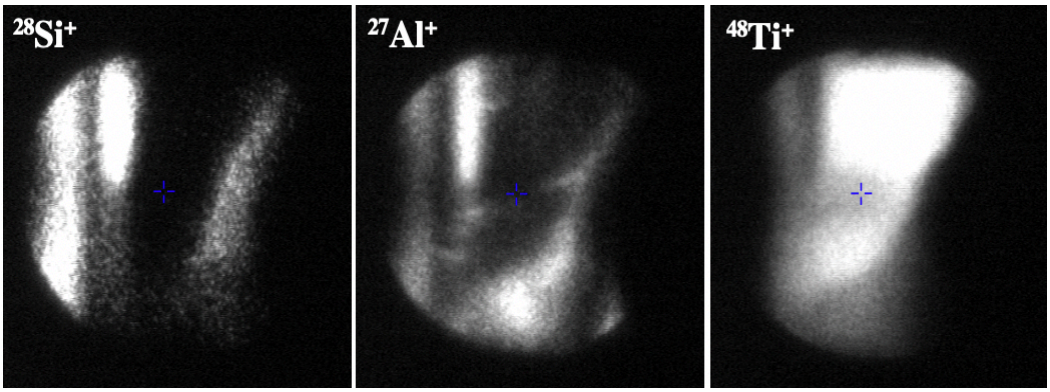

Figure 3.2.3. Secondary ion images of $^{27}Al^+$, $^{28}Si^+$, $^{48}Ti^+$ in sample QFM-1. Images were taken with a maximum image field of 75 μm. Note the dimmer region near the cross in the center of each image field. This is an artifact of the microchannel plate imaging system in that this area has been damaged when users allow too high of an ion current to strike this area. It does not represent a Ti-poor area within the crystal.

The secondary ion images shown in Figure 3.2.2. present a potential cause of the FWHM value for QFM-1 being larger than expected. The cross in the middle of the image represents the center of the area from which we collect secondary ions during analyses. The aluminum and silicon images represent a silicate phase that formed around the TiO_2 phase. With a 400 μm diameter field aperture inserted, the total analyzed area spans a diameter of 15 μm in the center of this image. However, it is possible that some

ions from the surrounding phase could have contributed to the energy spectrum resulting in a wider peak for $^{93}Nb^{+}$. For example, there is a faint trace of Al in Figure 3.2.2 cutting across the area of interest. If an insulating phase is sampled, the energy spectrum will broaden. Because the other samples allowed analyzes of areas that were unambiguously TiO_2, we are not considering sample QFM-1 in the rest of the discussion.

The spectra obtained on QFM and QFM+1 present both increasing peak width with increased sample fO_2. It is unclear why the spectrum of the Air at 1100˚C is snot significantly broader, but it is possible that the FWHM may reach a constant value (i.e., saturates) at some fO_2 between QFM+1 and QFM+8 (air at 1100˚C), similar to the effect of oxygen on the titanium energy spectra during addition of oxygen to Ti metal (Chapter 2).

While the results from these analyses might suggest this microanalytical technique is inapplicable to TiO_2, it is noted that if smaller steps than the current minimum of 1 V/step were accessible, one could obtain higher precision on the FWHM of these spectra than ±1 eV. This might enable sub-log-unit precision measurements of fO_2. The availability of larger crystals to analyze would also help confirm this promising early result.

Future work on this analytical application should include higher resolution energy spectra and the synthesis of larger rutile crystals at a range of fO_2 values between QFM+1 and air (e.g., QFM+2, +3, +4, etc.) to see if a plateau in the FWHM is indeed reached at high oxygen fugacities. Another ideal sample would be niobium-doped titanium metal, which could be studied to examine changes in the Nb energy spectra with

increasing oxygen coverage (also to search for saturation or a plateau in the FWHM). Samples synthesized at lower fO_2 (e.g., QFM-2, -3, -4, etc.) would also be useful to test if there is a similar plateau at reducing conditions.

3.3 ZONED ILMENITE

Xu et al. (2018) describes several generations of ilmenite formed by interaction with fluids resulting in the replacement of pre-existing ilmenite with other minerals (e.g., geikelite, eskolaite, rutile, chromite, etc.) along grain boundaries and cracks. Mineral replacements along grain boundaries suggests that the entire grain may not have been affected by metasomatism, providing a zone of varying ilmenite composition from the "core" to the "rim" of the grain.

An ilmenite megacryst (M7) acquired from a South African kimberlite mine showed such a variation in $Fe^{3+}/\sum Fe$ across the grain (based on electron microprobe data).

3.3.1 Analytical Methodology. Several locations across the grain were analyzed to identify any change in the FWHM of the $^{93}Nb^{+}$ energy spectra. The analyses were conducted at similar conditions as natural ilmenites discussed in Chapter 2. The mass resolving power was $M/\Delta M$ ~3000 (measured at $^{93}Nb^{+}$). The sample was sputtered with a primary ion beam of $^{40}Ar^{+}$ with ~45 nA beam current. The analysis was designed so the primary ion beam was rastered over an area of 50 x 50 μm^2, the maximum image field was 75 μm and the second field aperture was used to analyze a total diameter of 30 μm.

The analysis recipe is also written so that the sample energy is varied over a range of -20 eV to +60 eV (i.e., 4940-5020 eV). To reduce "noise" and increase the overall signal of the secondary ions, the integration time was increased. Analytical spots were chosen from the interior to the edge of the crystal after examining the secondary ion images of $^{27}Al^{+}$ and $^{28}Si^{+}$ to ensure no primary beam overlap on other phases (or epoxy).

After SIMS analyses of grain M7-1, electron microprobe analyses were performed at ASU to measure the hematite, ilmenite, and geikelite content of the entire grain as well as spot analyses near the SIMS craters and a traverse from the rim to the core of the grain.

3.3.2 Results. FWHM values calculated from the energy spectrum of niobium obtained from core to rim on M7-1 along with the calculated iron content (based on electron microprobe data) are shown below in Table 3.3.2.

Table 3.3.2

Electron Microprobe Data and Nb FWHM for M7-1 Ilmenite Sample

Analysis Spot	Calculated FWHM	Fe^{3+}/Fe^{2+}	$Fe^{3+}/\sum Fe$	Ilmenite (%)	Hematite (%)	Geikelite (%)
Rim (L)	25 eV	0.1897	0.1595	49.11	4.66	46.23
Rim (I)	26 eV	0.2042	0.1696	51.63	5.27	43.10
Rim (G)	28 eV	0.2278	0.1855	54.08	6.16	39.76
Core (C)	30 eV	0.2544	0.2028	60.58	7.70	31.72

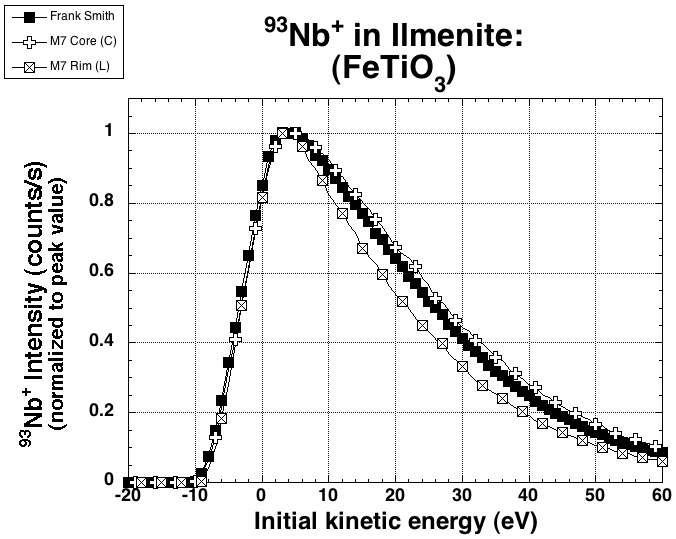

Figure 3.3.2. Energy spectrum of $^{93}Nb^{+}$ gathered on the core (spot C) and rim (spot L) of sample grain M7-1. Also shown in the $^{93}Nb^{+}$ energy spectrum for Frank Smith ilmenite. The peak intensities are normalized to 1 to better compare the peak widths.

These spectra shown in Figure 3.3.2 represent analyzed areas on the sample that had the most extreme difference in the calculated FWHM; the calculated FWHM of the core is 30 eV and the rim is 25 eV.

3.3.3 Discussion. Electron microprobe analyses of sample M7-1 were performed after SIMS analyses to measure the hematite content of the core and rim of this crystal. The electron microprobe work reveals a change in the hematite and ilmenite content from core to rim of the grain, but also shows that this ilmenite grain contains a variable geikelite ($MgTiO_3$) component. The rim of the grain contains up to 46% geikelite and the ilmenite (and hematite) content appears to increase toward the core of the grain. The average of the analyses is quite similar to the chemistry of the Frank Smith ilmenite in Chapter 2. The rim of M7-1 can be described as Mg- and Fe^{2+}-rich relative to the core.

The $FeTiO_3$, Fe_2O_3, and $MgTiO_3$ content of the core and rim of M7-1 are shown in a ternary diagram below in Figure 3.3.3.

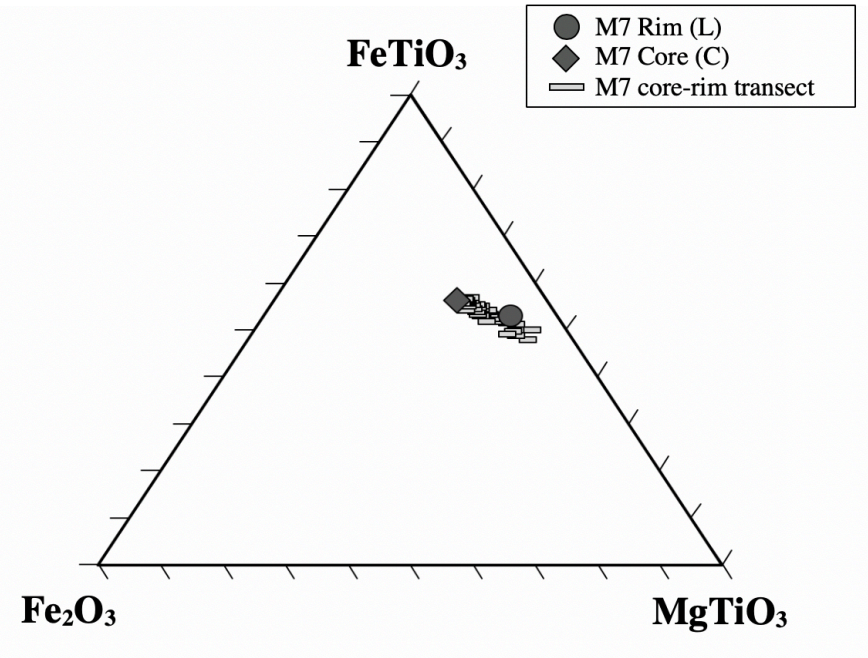

Figure 3.3.3. Ternary diagram of contents within the $FeTiO_3$-$MgTiO_3$-Fe_2O_3 mineral system. Individual electron microprobe spot analyses of M7-1 core and rim (near SIMS craters) are plotted as well as a transect line from the rim to the core of the M7-1 crystal.

Due to instrumental calibration reproducibility challenges, the energy spectrum of Nb sputtered from Frank Smith ilmenite, analyzed during the same session as M7-1, was examined. The energy spectrum of Frank Smith ilmenite was narrower than expected during this analytical session; this suggests the energy window was closed more than other analytical sessions. Although the spectra obtained were narrow, because Frank Smith was analyzed in the same session, the spectra of M7-1 can still be compared to the reference material.

The energy spectra of M7-1 in Figure 3.3.2 suggests there is a change in fO_2 along the grain from core to rim. The spectrum of the core (C) is slightly wider than the Frank Smith sample (formed at higher fO_2), but the spectra taken closer to the edge of the grain were similar or slightly narrower than the Frank Smith sample (lower fO_2). This change matches the electron probe data showing less Fe^{3+} toward the rim of the sample. The results from these analyses suggest this microanalytical technique is potentially applicable to zoned ilmenites, but it is important to study a reference material to be able to interpret the results.

3.4 CONCLUSIONS

The current state of this analytical technique is limited by the manufacturer's 1V step size when obtaining energy spectra but could be improved using a home-made power supply to make smaller steps. Another limitation is the size of the crystals to be analyzed, given that the technique uses niobium, a trace element in most rutile and ilmenite crystals. Yet another limitation is the lack of understanding of the exact relation between the FWHM and fO_2 (does this trend plateau at oxidizing or reducing conditions? Is it linear?). However, the bulk of our observations on the synthetic rutile and zoned ilmenite confirm the relation between increasing FWHM and fO_2 as determined in Chapter 2. The need for further study is expanded on in Chapter 4.

CHAPTER 4

DISCUSSION AND CONCLUSIONS

4.1 ANALYTICAL APPLICATIONS

Though the bulk of this study focuses on the application of this microanalytical technique to natural ilmenites formed at different oxidation potentials, there is a chance that this technique may be applied to a variety of materials—geologic or otherwise.

This technique is limited in that it is applicable only to conducting samples, and at present, insulating samples may not be analyzed under these analytical conditions. This is mostly due to the use of an Ar^+ primary ion beam. Insulating samples, like silicates, are best analyzed with a negative primary ion beam, such as O^-. The use of a positive primary ion beam (e.g., O^+, Ar^+, Cs^+) for analysis of insulating samples results in sample charging which impacts the overall secondary ion energy distributions. Although a metastable negative ion of Ar^- has been observed with a lifetime of 350±150 ns (Bae and Peterson, 1985), this ion would not be detected on the sample if such an analysis was attempted. As discussed in Chapter 2 of this study, the use of a primary ion beam of oxygen would contradict the purpose of this study; to analyze and measure the activity of oxygen within a sample.

At present, geologic applications of this technique are limited to conductive samples, but these materials are present in abundance throughout many geologic systems. Conductive sulfides and oxides are abundant in many volcanic systems and within complex systems like subduction zones. This technique could be used to determine the relative fO_2 within an individual crystal or an entire suite of rocks from a particular system or environment. Quantitative fO_2 measurements are not yet feasible, but future

investigations and experimental synthesis of a standard could make it possible to directly measure fO_2 within a geologic material.

There are potential applications of this technique in other fields such as materials science and engineering. In particular, when working with oxygen-sensitive devices, such as semiconductors or optical fiber devices, this technique could be applied to a reference material, such as a chip of U or Ta and used as a post-production control of oxygen content. The reference material would have to be held under the same conditions as the device (i.e., in the same instrument) to prevent any environmental contamination of the materials. As with geologic applications, a standard or pure reference material must be used when applying this technique to materials science.

4.2 FUTURE WORK

The microanalytical technique introduced throughout this thesis is far from complete and requires additional work to understand the effect of sample fO_2 on the behavior of secondary ions sputtered from a sample's surface.

Analytical Considerations. The bulk of this study focuses on applications of this technique to ilmenite crystals derived from a variety of environments. Any future SIMS analyses of ilmenite must consider chemical variations within a sample that may influence the peak shape of energy spectra. As seen in Chapter 3, ilmenite formed at different oxidation potentials can reflect variations in energy spectra, but the extent of the

influence these fO_2 variations have on energy spectra peak shapes is still unknown. Further work on this technique is needed to understand its full capabilities.

Determining what element to analyze throughout this study was also an important factor when trying to relate sample oxygen activity to the shape of its energy spectra. Though the spectra of zirconium in ilmenite was the inspiring force behind this study, low Zr contents in most ilmenite samples coupled with the challenge of separating the Zr peak from an intense molecular ion at the same nominal mass/charge limited our understanding of zirconium. In addition, while changes in the Zr spectrum were observed when sputtering variably oxidized Zr metal, no discernable difference was observed in natural ilmenites. As a result, it was not utilized for a large portion of this study. Oxygen backfill analyses on various semi-pure metals showed that at pressures from ~$1x10^{-8}$ torr to ~$5x10^{-6}$ torr, the increasing width of the energy spectra correlated with increasing crater floor oxygen coverage in Ta, Mo, and Nb. Unfortunately, due to the low abundance of Mo and Ta in natural ilmenites investigated in this study, energy spectra of Nb was utilized for identification of the oxygen activity within ilmenite. It would be best to study synthetic ilmenites formed at known fO_2 with enrichments of Ta, Nb, Zr, and Mo. A synthetic ilmenite would also provide a useful standard material that can be applied for quantitative fO_2 measurements.

Future work on this microanalytical technique should also incorporate applications of the technique to a multitude of other materials including (but not limited to) other minerals, experimental samples, and metals. Further investigation into the applicability of this technique should consider materials that are both conductive and have at least a minor enrichment in elements known to reflect some influence of fO_2 in

the secondary ion distribution energy (i.e., energy spectra). Conductive samples considered for analysis, at present, include sulfides, metals, Fe-rich spinels, and Ti-oxides such as ilmenite and TiO_2. Additionally, Zr-rich phases like baddeleyite (ZrO_2) have been considered (and analyzed) with this technique and show some influence of fO_2 on the energy spectra of Zr. Based on initial investigations, materials with abundant content of Zr, Nb, Ta, and Mo have shown the strongest correlation between secondary ion distributions over a range of oxidation conditions.

Furthermore, future work should also consider developing this technique for insulating materials. Silicate-rich minerals are far more abundant than conductive minerals in the accessible parts of our planet and the activity of oxygen within silicates also provides information about geologic systems. Insulating minerals like zircons, rich in elements known to reflect changes in secondary ion distributions based on sample oxygen activity, would be the best samples to focus on when beginning to tackle this issue.

Optimal Analytical Conditions. In addition to consideration of other elements and materials that may be applied to this technique, one must also ensure optimal analytical conditions. In Chapter 2 of this work, analytical conditions are discussed, but exactly reproducing the analysis conditions is a serious challenge. Throughout this study, analytical conditions were replicated as closely as possible between analytical sessions, but perhaps because of the non-automated nature of the instrument used, the energy spectra of the same mineral from session to session varies somewhat. Exactly reproducible instrument conditions would improve precision in the energy spectra from

session to session and reduce the overall error in each energy spectra measurement. A solution to the lack of reproducibility due to instrumental conditions is the use of a completely automated instrument. Newer SIMS instruments are becoming more and more automated, and this could help improve the overall reproducibility. Larger geometry instruments such as the Cameca 1280 and 1300 could also be utilized to allow higher transmission of trace elemental ions at the required high mass resolution for elements analyzed in this study, providing higher secondary ion count rates and thus better statistical errors than could be achieved in this study.

4.3 CONCLUSIONS

The microanalytical technique presented in this work focuses on measuring the secondary ion energy spectra of elements and oxides in various materials, specifically, in natural oxide minerals such as ilmenite. Energy spectra peak widths of $^{93}Nb^{+}$ in ilmenite display a strong correlation with the activity of oxygen in mantle-derived and meteoritic ilmenites. Although the technique presents a potential analytical tool to directly determine relative sample fO_2, minor changes in sample chemistry (e.g., the Fe:Mg ratio) could also influence the energy spectra peak width, and the influence of such minor components needs to be checked. In the absence of major element effects on the energy spectra, the results from analyses conducted throughout this study suggest that this microanalytical technique could be used to measure fO_2 variations within a single ilmenite grain or across a suite of ilmenite crystals. This thesis outlines some applications for this microanalytical technique, but continued work is necessary to determine the

potential applicability of this technique to be used for real-world geologic problems as well as materials science and material engineering purposes.

REFERENCES

Bae, Y. K., Peterson, J. R., Schlachter, A. S., & Stearns, J. W. (1985). Observation of the metastable negative argon ion Ar−. *Physical review letters*, *54*(8), 789.

Boyd, & Nixon. (1975). Origins of the ultramafic nodules from some kimberlites of northern Lesotho and the Monastery Mine, South Africa. *Physics and Chemistry of the Earth, 9*(C), 431-454.

Buddington, A. F., & Lindsley, D. H. (1964). Iron-titanium oxide minerals and synthetic equivalents. *Journal of petrology*, *5*(2), 310-357.

Cain, F. (2016). What is the earth made of? *Universe Today*. Retrieved from https://www.universetoday.com/40229/what-is-the-earths-mantle-made-of/

Castaing, R., & Slodzian, G. (1962). Microanalyse par èmission ionique secondaire. *Journal de microscopie, 1*, 395-410.

Castaing, R., & Slodzian, G. (1981). Analytical microscopy by secondary ion imaging techniques. *Journal of Physics E: Scientific Instruments*, *14*(10), 1119.

Dawson, J. B. (1980). The Megacryst Suite. In *Kimberlites and Their Xenoliths* (pp. 190-199). Springer, Berlin, Heidelberg.

Dawson, J. B. (1984). Contrasting types of upper-mantle metasomatism?. In *developments in petrology* (Vol. 11, No. 2, pp. 289-294). Elsevier.

Dawson, J. B., & Smith, J. V. (1977). The MARID (mica-amphibole-rutile-ilmenite-diopside) suite of xenoliths in kimberlite. *Geochimica et Cosmochimica Acta*, *41*(2), 309-323.

Frost, B. R. (1991a). Introduction to oxygen fugacity and its petrologic importance. *Reviews in Mineralogy and Geochemistry*, *25*(1), 1-9.

Frost, B. R. (1991b). Stability of oxide minerals in metamorphic rocks. *Reviews in Mineralogy and Geochemistry*, *25*(1), 469-487.

Frost, B. R., & Lindsley, D. H. (1991). Occurrence of iron-titanium oxides in igneous rocks. *Reviews in Mineralogy and geochemistry*, *25*(1), 433-468.

Gnaser, H., & Hutcheon, I. D. (1987). Velocity-dependent isotope fractionation in secondary-ion emission. *Physical Review B*, *35*(2), 877.

Haggerty, S. E. (1976). Opaque mineral oxides in terrestrial igneous rocks. *Reviews in Mineralogy*, *3(1),* 101-300.

Haggerty, S. E. (1991). Oxide mineralogy of the upper mantle. *Oxide minerals: petrologic and magnetic significance*, 355-416.

Haggerty, S. E. (1995). Upper mantle mineralogy. *Journal of Geodynamics*, *20*(4), 331-364.

Haggerty, S. E., & Tompkins, L. A. (1983). Redox state of Earth's upper mantle from kimberlitic ilmenites. *Nature*, *303*(5915), 295-300.

Hervig R., Dillon S., and Williams P. (2018) SIMS microanalysis for fO_2. *Int. Goldschmidt Conference,* 2018.

Hinton, R. W., & Long, J. V. P. (1979). High-resolution ion-microprobe measurement of lead isotopes: Variations within single zircons from Lac Seul, northwestern Ontario. *Earth and Planetary Science Letters*, *45*(2), 309-325.

Hunter, L., Gordon, J., Peck, S., Ang, D., & Lin, J. (2013). Using the Earth as a polarized electron source to search for long-range spin-spin interactions. *Science (New York, N.Y.),339*(6122), 928-932.

Lauterbach, S., McCammon, C. A., Van Aken, P., Langenhorst, F., & Seifert, F. (2000). Mössbauer and ELNES spectroscopy of (Mg, Fe)(Si, Al)O_3 perovskite: a highly oxidised component of the lower mantle. *Contributions to Mineralogy and Petrology*, *138*(1), 17-26.

McCammon, C. A., Frost, D. J., Smyth, J. R., Laustsen, H. M. S., Kawamoto, T., Ross, N. L., & Van Aken, P. A. (2004). Oxidation state of iron in hydrous mantle phases: implications for subduction and mantle oxygen fugacity. *Physics of the Earth and Planetary interiors*, *143-144*, 157-169.

McDonough, W. F., & Rudnick, R. L. (1998). Mineralogy and composition of the upper mantle. *Reviews in mineralogy*, *37(1)*, 139-164.

Meuller, P. & Vervoort, J. (2017). Secondary ion mass spectrometer (SIMS) [Web page]. Retrieved from https://serc.carleton.edu/research_education/geochemsheets/techniques/SIMS.html

Mitchell, R. H. (1986). Kimberlites and related rocks. *Kimberlites: mineralogy, geochemistry, and petrology* (pp. 9-28). New York, NY: Springer.

Morgan, A. E., & Werner, H. W. (1977). Quantitative SIMS studies with a uranium matrix. *Surface Science*, *65*(2), 687-699.

O'Neill, H. S. C., & Wall, V. J. (1987). The Olivine-Orthopyroxene-Spinel oxygen geobarometer, the nickel precipitation curve, and the oxygen fugacity of the Earth's Upper Mantle. *Journal of Petrology*, *28*(6), 1169-1191.

Patterson, M. V., & Francis, D. (2013). Kimberlite eruptions as triggers for early Cenozoic hyperthermals. *Geochemistry, Geophysics, Geosystems*, *14*(2), 448-456.

Powell, R., & Powell, M. (1977). Geothermometry and oxygen barometry using coexisting iron-titanium oxides: a reappraisal. *Mineralogical Magazine*, *41*(318), 257-263.

Rudat, M. A., & Morrison, G. H. (1979). A computerized system for determining secondary ion energy spectra. *Analytica Chimica Acta*, *112*(1), 1-9.

Slodzian, G. (1975). Some problems encountered in secondary ion emission applied to elementary analysis. *Surface Science*, *48*(1), 161-186.

Ulff-Møller, F. (1985). Solidification History of the Kitdl t Lens: Immiscible Metal and Sulphide Liquids from a Basaltic Dyke on Disko, Central West Greenland. *Journal of Petrology, 26*(1), 64-91.

White, W. M. (2013). Geochemistry of the solid earth. *Geochemistry* (pp. 484-552). Hoboken, NJ: John Wiley and Sons.

Williams, P., & Hervig, R. (Eds.). (2000). Proceedings of the twelfth international conference on secondary ion mass spectrometry (SIMS XII): *Associative detachment reactions in oxygen-sputtered uranium*. Amsterdam, NH: Elsevier.

Wood, B. J. (1991). Oxygen barometry of spinel peridotites. *Reviews in Mineralogy*, *25*, 417-431.

Xu, J., Melgarejo, J. C., & Castillo-Oliver, M. (2018). Ilmenite as a recorder of kimberlite history from mantle to surface: examples from Indian kimberlites. *Mineralogy and Petrology*, *112*(2), 569-581.

Zinner, E., & Crozaz, G. (1986). A method for the quantitative measurement of rare earth elements in the ion microprobe. *International Journal of Mass Spectrometry and Ion Processes*, *69*(1), 17-38.

APPENDIX A

PRELIMINARY EARTH REFERENCE MODEL

The Preliminary Reference Earth Model (PREM) of seismic velocities and density variations through the Earth.

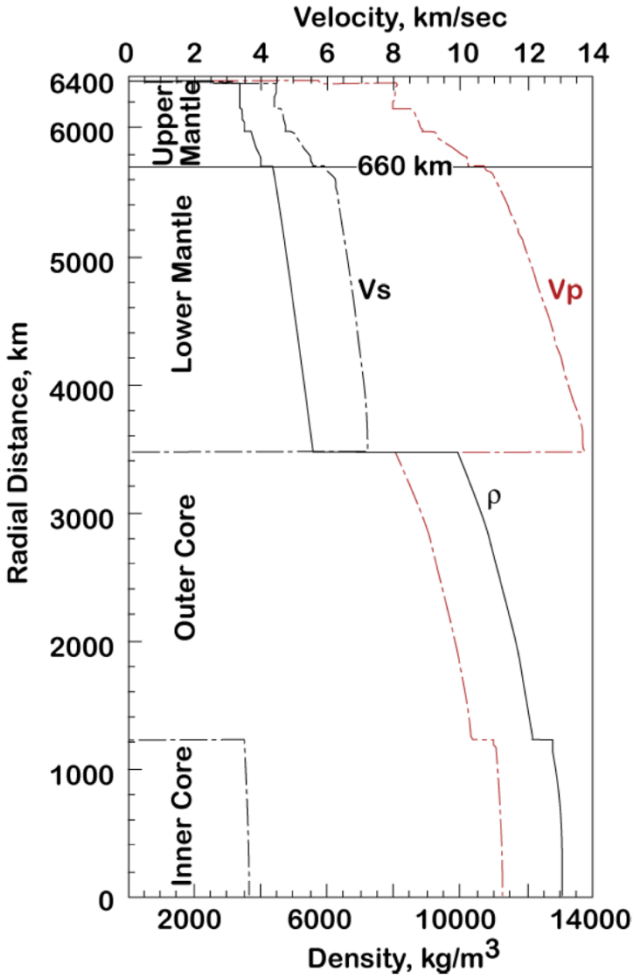

(copied from White, 2013).

APPENDIX B

MANTLE MINERALOGY

Mineral proportions in the pyrolite model as a function of depth (A) and the resulting iron and electron densities in the various electronic spin states (B).

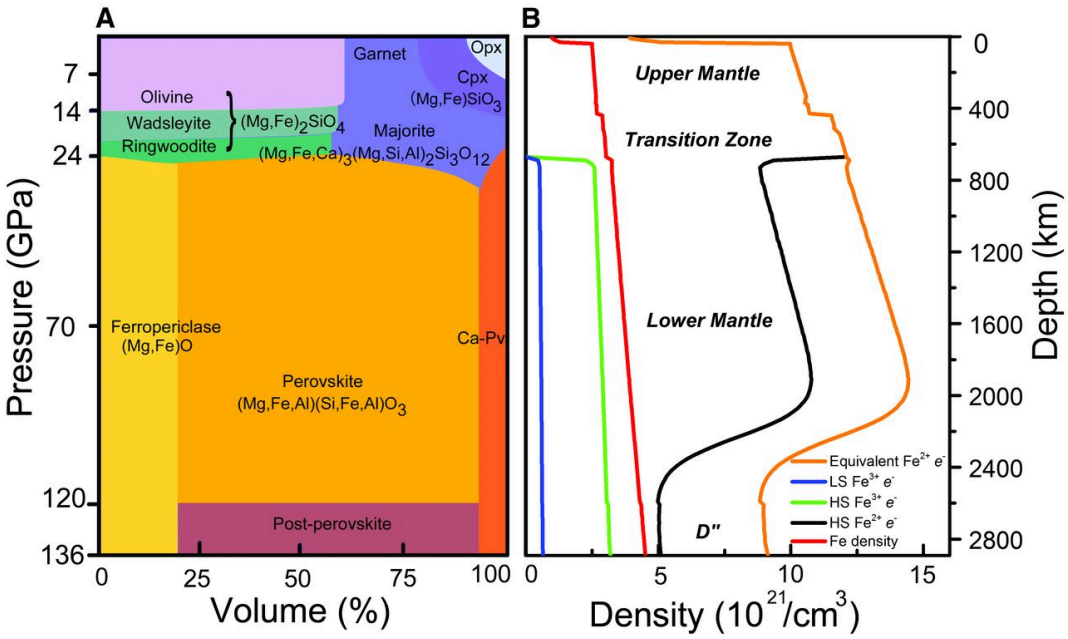

(copied from Hunter, Gordon, Peck, Ang, & Lin, 2013).

Mineral assemblages in the upper 1000 km of the mantle.

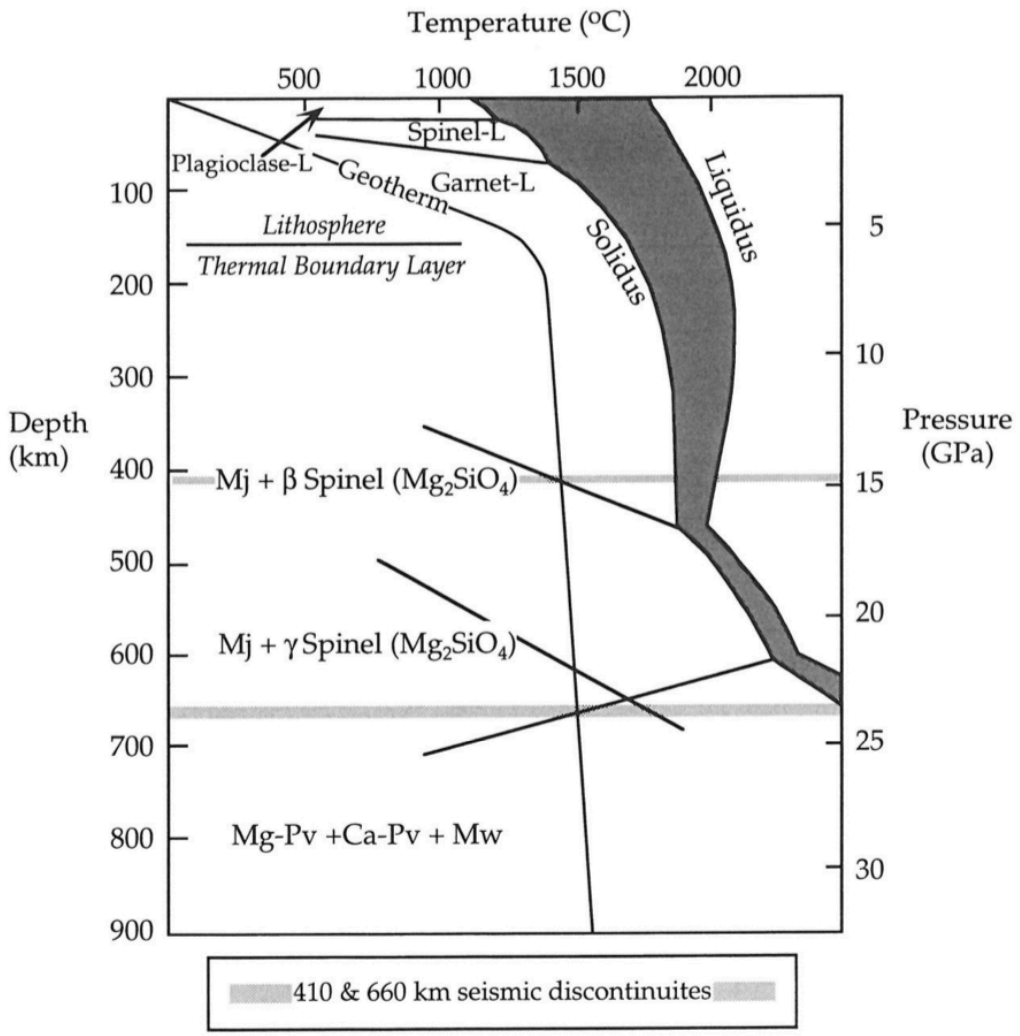

(copied from McDonough, & Rudnick, 1998)

APPENDIX C

MASS SPECTROMETRY TERMINOLOGY

Mass-to-charge ratio (m/z):

The x-axis of a plotted mass spectrum (see figure 2.1.6) is often labeled in units of m/z, where m denotes the mass of the ion (in Daltons), and z represents the total number of charges on the ion (in units of the elementary charge).

Resolution (ΔM/M):

Resolution can be defined in many ways but is most commonly defined by the formula ΔM/M, where ΔM is defined as the peak width at 5% of the peak maximum.

Two adjacent, symmetrical peaks of equal height at masses M and M-ΔM are considered separated if the valley between them is just 10% of the peak heights.

FWHM:

FWHM resolution is still calculated as ΔM/M, but now ΔM is the width of the peak at half (50%) of the peak height.

Resolving power (M/ΔM):

Resolving power is simply the inverse of resolution.